

Performance-Optimized Quantization for SAR and InSAR Applications

Michele Martone, Nicola Gollin, Paola Rizzoli, and Gerhard Krieger, *Fellow, IEEE*

Abstract—For the design of present and next-generation spaceborne SAR missions, constantly increasing data rates are being demanded, which impose stringent requirements in terms of onboard memory and downlink capacity. In this scenario, the efficient quantization of SAR raw data is of primary importance, since the utilized compression rate is directly related to the volume of data to be stored and transmitted to the ground and, at the same time, it affects the resulting SAR imaging performance. In this paper, we introduce the performance-optimized block-adaptive quantization (PO-BAQ), a novel approach for SAR raw data compression which aims at optimizing the resource allocation and, at the same time, the quality of the resulting SAR and InSAR products. This goal is achieved by exploiting the a priori knowledge of the local SAR backscatter statistics, which allows for the generation of high-resolution bitrate maps that can be employed to fulfill a predefined performance requirement. Analyses on experimental TanDEM-X interferometric data are presented, which demonstrate the potentials of the proposed method as a helpful tool for performance budget definition and data rate optimization of present and future SAR missions.

Index Terms—Synthetic aperture radar (SAR), block adaptive quantization (BAQ), Interferometric SAR (InSAR), data volume optimization.

I. INTRODUCTION

SYNTHETIC aperture radar (SAR) represents nowadays a well-recognized technique for many remote sensing applications, as it is able to acquire high-resolution images independent of daylight and weather conditions. Interferometric SAR (InSAR) exploits the phase difference of (at least) two complex SAR images, which are acquired from different orbit positions and/or at different times. Since the pioneering experiments carried out by NASA-JPL using data acquired by the SEASAT sensor in the late 1970s [1] and the first practical demonstration of InSAR for measuring crustal deformation caused by the 1992 Landers earthquake [2], about forty years of research studies, technical progress, and developments have demonstrated the potential of spaceborne InSAR systems for the assessment and monitoring of many geophysical parameters, such as ocean currents, ground deformations, and Earth’s topography, through the generation of digital elevation models (DEMs). In 2000, the Shuttle Radar Topography Mission (SRTM) delivered the first elevation data on a nearly global scale [3]. Ten years later, the German Aerospace Center (DLR) TerraSAR-X SAR satellite (launched in 2007) was enhanced by its twin radar satellite TanDEM-X

(launched in 2010) to begin the TanDEM-X (TerraSAR-X add-on for Digital Elevation Measurement) mission, opening a new era in spaceborne radar remote sensing [4], [5]. In the last years, innovative spaceborne radar techniques have been introduced to overcome the limitations imposed by “conventional” SAR imaging for the acquisition of wider swaths and, at the same time, of finer azimuth resolutions. As an example, single-azimuth-channel SAR based on the simultaneous recording of multiple echo pulses received from different directions (so-called “multibeam” mode) [6], [7] enables an increase of the imaged area by keeping a reduced antenna size and avoiding the employment of burst modes. Alternatively, multiple azimuth channels (MAC) and digital beamforming (DBF) in elevation can be applied to achieve Scan-on-Receive (SCORE) [8], [9], [10], [11], [12], [13]. The idea of exploiting the variation of the pulse repetition interval (PRI) to solve the blind range problem (which arise since the radar cannot receive while transmitting) was first proposed independently in [14] and in [6], [15] and then culminated in the staggered SAR concept, which includes a refined design of the PRI sequences and proper interpolation of the raw data [16], [17]. In this way, high-resolution imaging of a large continuous swath of up to several hundreds of kilometers, without the need for a long antenna with multiple apertures, becomes possible [16]. Another step forward is represented by the development of the multi-channel staggered SAR concept, which combines the strengths of SCORE with multiple elevation beams and staggered PRI, as well as multiple channels in azimuth, allowing for a further improvement of the resolution and swath width achievable by the system [18], [19].

Such significant developments in terms of system capabilities, in combination with the employment of large bandwidths and multiple acquisition channels, are clearly associated with the generation of a large volume of data to be gathered in a shorter time interval, which, in turn, implies harder requirements for the onboard memory and downlink capacity of the sensor. In this scenario, the proper quantization of SAR raw data is of utmost importance, as it defines, on the one hand, the amount of onboard data and, on the other hand, it directly affects the performance of the SAR products. These two aspects must be traded off due to the constrained acquisition capacity of the system.

Nowadays, one of the most widely used methods for SAR raw data digitization is the block-adaptive quantization (BAQ), further detailed in Section II. In the last years, novel algorithms have been proposed, allowing for a finer performance and resource optimization, based on data-driven

The authors are with the Microwaves and Radar Institute, German Aerospace Center (DLR), 82234 Wessling, Germany. e-mail: Michele.Martone@dlr.de

compression schemes [20], [21], [22], and combined with the implementation of non-integer data rates [23]. SAR systems are often designed so that a certain degree of correlation and redundancy is present in the acquired raw data, hence opening up new opportunities for efficient onboard data volume reduction, as introduced in the context of conventional SAR [24], [25], [26], as well as multi-channel [27], [28] and staggered SAR systems [29], [30].

In this paper a novel performance-optimized block-adaptive quantization (PO-BAQ) is introduced, which extends the concept of the state-of-the-art BAQ and allows for an optimization of the resource allocation by controlling the resulting SAR image degradation. Since quantization errors are significantly influenced by the local distribution of the SAR intensity, such an optimization is achieved by exploiting the a priori knowledge about the SAR backscatter statistics of the imaged scene. In view of systematic mapping missions like Sentinel-1 [31], [32], [33], Tandem-L [34], [35], and especially ROSE-L [36], [37], and Sentinel-1 NG [38], [39], selected areas are or will be mapped repeatedly with a temporal sampling down to one week, such that up-to-date backscatter maps are always available. Given the severe constraints imposed by the downlink capacity, the approach and analyses presented in this paper may help to optimize the overall global performance for a given downlink budget.

The paper is organized as follows: a short overview on quantization errors in SAR imaging as well as on the key parameters considered for the assessment of quantization effects on SAR and InSAR performance is provided in Section II. Section III investigates the effects of quantization on TanDEM-X interferometric SAR data for a variety of terrain characteristics and inhomogeneities in the backscatter response. Based on the obtained results, PO-BAQ is introduced in Section IV and its potentials are demonstrated, at global as well as local scale, by exploiting backscatter maps generated from TanDEM-X data. Finally, Section V concludes the paper.

II. SAR RAW DATA QUANTIZATION AND PERFORMANCE

The digitization of an analog signal is an irreversible process which leads to an information loss, as the reconstructed signal \hat{x} is a distorted version of the input signal x , depending on the selected bitrate and on the specific quantization scheme. The difference between the input and the corresponding output signal is therefore referred to as *quantization error* q

$$q = x - \hat{x}. \quad (1)$$

This error contribution is deterministic, since, for a given input, always the same (single) output is returned. On the other hand, if the input x has a random nature, the error q can be reasonably modeled as an additive and signal-correlated random noise contribution [40].

A. BAQ and Quantization Errors

Block-adaptive quantization (BAQ) is a lossy data compression method which employs a space-varying estimation of the raw data blocks to set up the quantizer dynamic. This information is then exploited to determine

the quantization decision levels that best match with the observed backscatter statistics [41], [42]. Being a simple scalar quantizer, BAQ offers a good trade-off between scheme complexity, achievable compression ratio, and resulting image quality. For these reasons, it represents an attractive solution for data quantization in spaceborne SAR systems, where a large amount of on-board data needs to be stored and then transmitted to the ground. In the last years, novel quantization algorithms have been proposed, allowing for a finer performance and resource optimization, by means of the implementation of non-integer compression rates [20], [21], [22], [23].

For what concerns quantization errors, they are typically given by the sum of two contributions: the granular noise and the overload noise. The former is due to the reduced number of output decision levels within the supported dynamic range, while the latter is introduced by the clipping of input signals exceeding the supported range. Clearly, the fewer bits are employed for data compression, the higher is the quantization noise power affecting the SAR image quality.

Moreover, inhomogeneities in the SAR backscatter distribution cause a further signal-dependent performance degradation. This is the case, for example, of urban areas, where a high dynamic range in backscatter is typically observed. Such an effect is also referred to as low-scatterer suppression [43], [44] and has to be considered as an additional, non-linear and signal-dependent quantization error source (different from granular and clipping noise, since it is visible only after SAR focusing), and it significantly impairs the resulting SAR image performance. Indeed, in a SAR acquisition the responses of the scatterers under illumination overlap in the raw data domain within an area

$$A_{\text{SAR}} = L_{\text{chirp}} \times L_s. \quad (2)$$

L_{chirp} is the chirp length projected in ground range and L_s is the azimuth synthetic aperture, which, in turn, are defined as

$$L_{\text{chirp}} = \frac{c\tau_p}{2 \cdot \sin(\theta_i)}, \quad (3)$$

$$L_s = \lambda \frac{R}{L_a}, \quad (4)$$

being c the light velocity, τ_p the chirp pulse duration, R the slant range distance, θ_i the incidence angle, and L_a the azimuth antenna length. In addition to that, the scatterer responses are opportunely weighted by the azimuth and elevation antenna patterns. According to the BAQ algorithm, the decision levels and the clipping thresholds for the compression are determined with respect to the mean power of the raw data block. Therefore, if two overlapping targets have different magnitude responses and are distant in range d_r and azimuth d_a with

$$d_r \ll L_{\text{chirp}}, \quad d_a \ll L_s, \quad (5)$$

then the stronger signal will be better reconstructed, while the lower one is heavily distorted [44]. In this sense, quantization errors are to be treated as a non-linear and signal-dependent error source affecting the SAR data, for which the correlation between noise and data must be accounted for the proper performance modeling. In addition to the compression rate N_b

used for data digitization, the degree of inhomogeneities in the backscatter distribution can therefore be exploited to quantify and predict the impact of quantization on SAR performance. A possibly good estimator of this is represented by the standard deviation of the local SAR backscatter σ_{σ^0} . According to this, a lower performance degradation is expected for homogeneous scenes (corresponding to low values of σ_{σ^0}) and vice-versa. The impact of the described low-scatterer suppression on several SAR performance descriptors is discussed in [43], [44] and further investigated in Section III. The obtained results represent the basis for the proposed PO-BAQ, which is introduced in Section IV.

B. SAR and InSAR Performance Descriptors

In this section the most relevant parameters considered for evaluating the impact of quantization on SAR and InSAR performance are recalled.

The *signal-to-quantization noise ratio* (SQNR) represents the figure of merit of a quantizer which describes how much the output signal has been corrupted by quantization noise. According to (1), it is defined as the power ratio of the input x to the quantization error q and for a complex SAR image it is calculated as

$$\text{SQNR} = \frac{\sigma_x^2}{\sigma_q^2} = \frac{\sum_{p=1}^P |x_p|^2}{\sum_{p=1}^P |q_p|^2}, \quad (6)$$

being P the total number of image pixels.

Moving to InSAR performance, the *quantization correlation factor* γ_q describes the coherence loss due to quantization, i.e., the amount of noise affecting the SAR interferogram due to raw data compression (with coherence $\gamma_{\hat{x}}$) with respect to the uncompressed interferogram with coherence γ_x

$$\gamma_q = \frac{\gamma_{\hat{x}}}{\gamma_x} = \frac{1}{1 + \frac{1}{\text{SQNR}}} = \frac{\text{SQNR}}{\text{SQNR} + 1}. \quad (7)$$

The last two terms express the relation between γ_q and SQNR, which holds provided that the SQNR of the two interferometric channels is approximately the same. One can derive an expression of the SQNR alternative to (6) by inverting (7) as

$$\text{SQNR} = \frac{\gamma_q}{1 - \gamma_q}. \quad (8)$$

The percent coherence loss due to quantization $\Delta\gamma_q$ is obtained from γ_q simply as

$$\Delta\gamma_q = 100 \cdot (1 - \gamma_q). \quad (9)$$

Furthermore, *interferometric phase errors* are directly related to the coherence and to the equivalent number of looks N_1 employed within the multilooking process [4], [45]. The impact of raw data quantization on the interferometric phase is evaluated by comparing the phase of the non-compressed interferogram φ_x with the one generated at a different BAQ rate $\varphi_{\hat{x}}$

$$\Delta\varphi_q = \varphi_x - \varphi_{\hat{x}}. \quad (10)$$

The differential interferogram $\Delta\varphi_q$ is nominally confined in the interval $[-2\pi, 2\pi]$. However, the maximum real phase error

TABLE I
SYSTEM PARAMETERS FOR THE TANDEM-X MISSION.

Parameter	Value
Satellite height (equator), h_s	514 km
Carrier frequency, f_c	9.65 GHz
Radar wavelength, λ	3.11 cm
Chirp bandwidth, B_{rg}	100 MHz
Chirp pulse duration, τ_p	10 - 60 μs
Antenna length, L_a, L_e	4.8 m (azimuth), 0.8 m (elevation)
Incidence angles, θ_i	29° - 48°
Available BAQ rates, N_b	2, 3, 4, 6, 8 bits/sample
Satellite memory	TerraSAR-X: 256 Gbit, TanDEM-X: 512 Gbit
Downlink capacity	~260 Mbits/s (total net data rate)

achievable is equal to $\pm\pi$, and all possible values outside the interval $[-\pi, \pi]$ are wrapped symmetrically around the corresponding bound, so that the interferometric phase errors due to quantization can be finally expressed as:

$$\Delta\varphi_q = \begin{cases} \Delta\varphi_q, & \text{if } |\Delta\varphi_q| \leq \pi; \\ -\text{sign}(\Delta\varphi_q) \cdot (2\pi - |\Delta\varphi_q|), & \text{if } |\Delta\varphi_q| > \pi. \end{cases} \quad (11)$$

In general, $\Delta\varphi_q$ has zero mean, independently of the used quantization rate, while its standard deviation $\sigma_{\Delta\varphi_q}$ gives information about the dispersion of the interferometric phase errors and it is considered in the following for performance assessment purposes.

III. TANDEM-X DATA ANALYSIS

After a short overview of the TanDEM-X mission, this section presents the impact of SAR raw data quantization on interferometric TanDEM-X SAR/InSAR performance, with particular focus on the relation between quantization errors and SAR backscatter characteristics and statistics.

A. Overview of the TanDEM-X Mission

TanDEM-X (TerraSAR-X add-on for Digital Elevation Measurement) is the first operational spaceborne bistatic SAR system, which comprises two X-band SAR satellites. Developed under a public-private partnership between the German Aerospace Center (DLR) and Airbus Defense & Space [4], [46], the TerraSAR-X SAR satellite (launched in 2007) is enhanced by its twin radar satellite TanDEM-X (launched in 2010). A list of the main TanDEM-X system parameters is given in Table I. Since end of 2010, the two satellites have been operationally acquiring interferometric SAR images in stripmap single horizontal (HH) polarization mode, with a typical resolution of about 3 meters in azimuth and range. Both satellites fly in a closely controlled orbit formation with the opportunity for flexible along- and across-track baseline selection with the primary objective of generating a global, consistent and high-precision digital elevation model (DEM) [4] at a final independent posting of 12 m \times 12 m. Nominal acquisitions are provided in bistatic SAR acquisition mode, where either TerraSAR-X or TanDEM-X is used as transmitter (master) and both satellites (master and slave) simultaneously record the signal scattered back from the Earth's surface. TanDEM-X provides the community with a unique data set to be exploited for a wide

TABLE II

LIST OF TEST AREAS FOR THE ANALYSIS ON TANDEM-X DATA. FOR THE DERIVATION OF σ_{σ^0} , PIXELS WITH $\gamma_x < 0.4$ ARE NOT CONSIDERED.

Test Site	σ_{σ^0}
Greenland - snow & ice, flat	1.6 dB
Iowa (USA) - agricultural, flat	2.3 dB
Amazonas (Brazil) - rainforest, flat	2.7 dB
Mato Grosso (Brazil) - rainforest with clear-cuts, flat	3.1 dB
Death Valley (USA) - soil & rock, mountainous	3.7 dB
Naples (Italy) - urban & terrain, mountainous	4.0 dB
Las Vegas (USA) - urban, flat	4.2 dB
Mexico City (Mexico) - urban, mountainous	4.6 dB
Malaysia - tropical forest, mountainous	4.8 dB

range of commercial as well as scientific applications [47]. The global TanDEM-X DEM has been finalized and delivered in September 2016 [5], and a DEM at 90-meter resolution has been released for scientific use and is available as a global dataset [48]. Since the beginning of the mission, more than half a million high-resolution bistatic scenes (two global mappings of the Earth's landmasses plus additional acquisitions over selected regions, such as mountainous terrain, forested areas, or sandy desert regions, to improve the overall product accuracy), typically extending over an area of about 30 km in range by 50 km in azimuth, have been acquired and processed, with interferometric baselines B_{\perp} in the range between 80 m and 500 m.

On board of the TerraSAR-X and TanDEM-X satellites, the received backscattered signal is first digitized by an 8-bit analog-to-digital converter (ADC) and then further compressed by a block adaptive quantizer (BAQ), which has been introduced in Section II-A. For the space-varying estimation of raw data statistics, blocks of fixed size of $N_{\text{block}} = 128$ range samples are used, for the in-phase (I) and quadrature (Q) channels, separately. This information is then used to define the quantization decision levels which best match with the observed statistics. Possible compression rates are 2, 3, 4, 6, and 8 bits/sample, where the latter corresponds to BAQ bypass [49]. The compression rate is individually configured before every data take by instrument commanding and is kept constant for the whole acquisition. For example, for the acquisition of the TanDEM-X global DEM, BAQ at 3 bits/sample was mainly used, as it offers a good trade-off between the achievable data rate and the resulting image quality [4], [44]. For the raw data acquired by the TanDEM-X SAR satellites, the granular noise can be considered as the dominant error source caused by quantization, as the instrument parameters are set to minimize the occurrence of saturation effects [49]. In addition to that, low-scatterer suppression intrinsically affects TanDEM-X SAR products, as explained in Section II-A and further detailed in Section III-B (for TanDEM-X, typical values of L_s and L_{chirp} are in the order of a few kilometers). While being a very flexible and powerful system, the acquisition capabilities of the TerraSAR-X and TanDEM-X satellites are constrained by their relatively short orbit duty cycle (about 3 minutes per orbit), limited on-board memory (of 256 Gbit and 512 Gbit, respectively), and, ever more critical, by the limited downlink capacity provided by the ground station network, which pose

TABLE III

ACQUISITION PARAMETERS FOR THE TWO TANDEM-X SCENES OVER IOWA (USA) AND MEXICO CITY (MEXICO) SHOWN IN FIG. 1.

Test Site	Iowa	Mexico City
Land cover	Agricultural, flat	Urban, flat
Center coordinates [lat./lon.]	[41.7°N, 93.1°W]	[19.4°N, 99.1°W]
Acquisition date	2010-11-10	2012-02-29
Incidence angle, θ_i	33.7°	33.7°
Backscatter std dev, σ_{σ^0}	2.3 dB	4.6 dB
Acquisition mode	Bistatic, stripmap	
Polarization channel	HH	

constraints on the achievable data rate during the mission: indeed, about one year was required to complete one global acquisition of the Earth's landmasses fulfilling the mission specifications [4], [5].

B. Assessment of Quantization Effects

We evaluated the impact of quantization on TanDEM-X SAR bistatic data over selected test areas showing different land cover types and topography characteristics, which are summarized in Table II. Each test site has been acquired once in stripmap configuration, HH polarization with single-look resolution of about 3 m in azimuth and ground range (the acquisition date was between 2010 and 2012). In the table, the standard deviation of the log-backscatter distribution for the corresponding SAR image σ_{σ^0} is provided as well. For its derivation each image pixel is computed as

$$\sigma^0 = 10 \cdot \log_{10} (\beta^0 \cdot \sin(\theta_i)), \quad (12)$$

being β^0 the calibrated radar brightness (SAR intensity) and θ_i the local incidence angle, and out of this the standard deviation is evaluated. It is worth pointing out that the backscatter statistics have been derived from an averaged (multi-looked) version of the original single-look TanDEM-X SAR backscatter σ^0 (as in (12)) at a final resolution of 12 m \times 12 m in azimuth and ground range, respectively, for consistency with the coherence and phase maps, which are also generated at the same independent posting. The experimental TanDEM-X data takes, acquired with full 8-bit analog-to-digital converter (ADC) resolution, have been re-compressed on ground using BAQ at the available rates. Then, the corresponding SAR images and interferograms have been generated by using the experimental TanDEM-X interferometric processor (TAXI), developed at DLR [50]. The combination of different compression rates for the master and the slave acquisitions allows for the implementation of non-integer BAQ rates (e.g., 3-bit BAQ for the master and 2-bit BAQ for the slave leads to an equivalent 2.5-bit for the resulting interferometric products) [44]. Fractional quantization rates can be implemented as well by toggling the integer BAQ rate along azimuth (and/or range) as described in [23]. The signal-to-quantization noise ratio (SQNR), the coherence loss, and the interferometric phase errors, introduced in Section II-B, are considered in the following for the performance assessment.

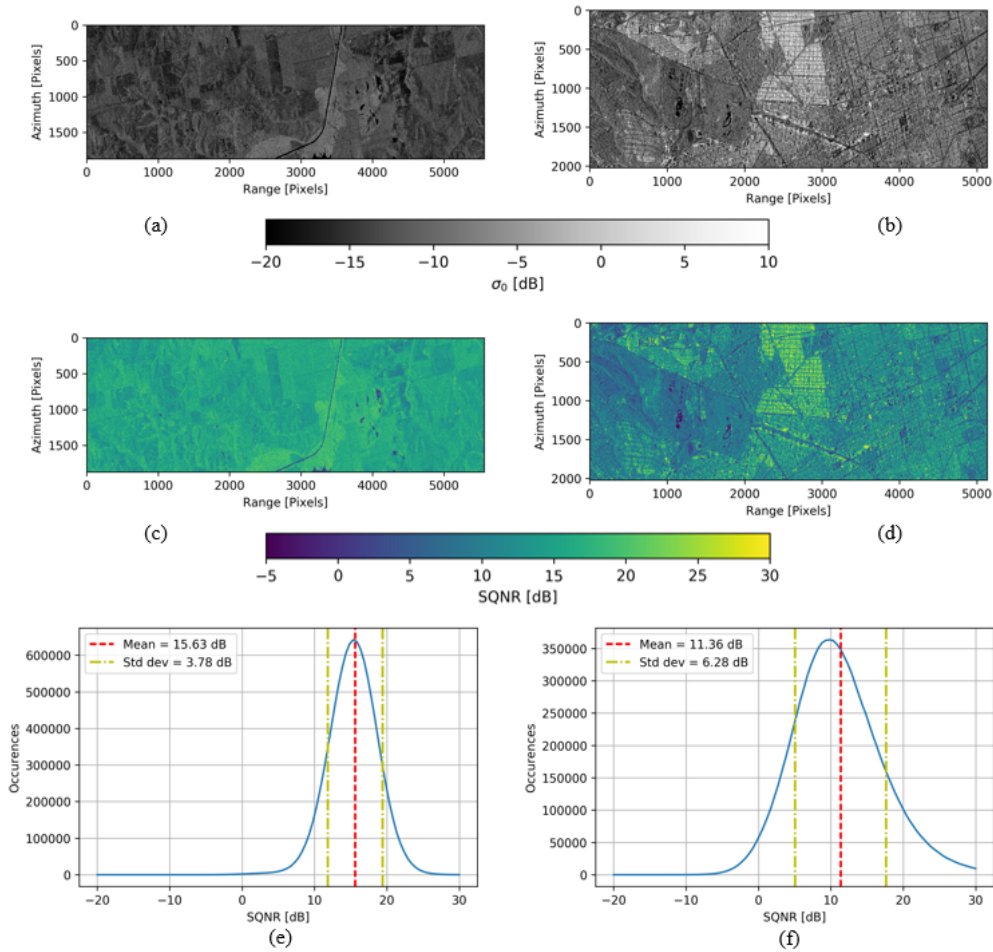


Fig. 1. Zoom-in of the radar backscatter map σ^0 for (a) the homogeneous test area located in Iowa (USA) (σ_{σ^0} of about 2 dB) and (b) of the urban area of Mexico City (σ_{σ^0} of 4.5 dB); (c), (d) SQNR maps resulting from 3-bit BAQ and (e), (f) corresponding SQNR distributions.

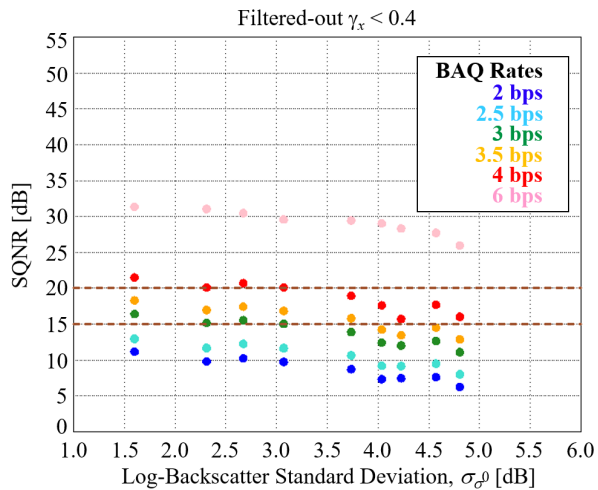


Fig. 2. Mean SQNR (derived as in (8)) as a function of the standard deviation of the radar backscatter σ_{σ^0} for different BAQ rate configurations. Each value of σ_{σ^0} corresponds to a different test site (listed in Table II). For the derivation of σ_{σ^0} and of the mean SQNR, pixels with $\gamma_x < 0.4$ are filtered out. The two horizontal brown lines trace exemplary SQNR requirements of 15 dB and 20 dB, which are considered later on for the application of the PO-BAQ.

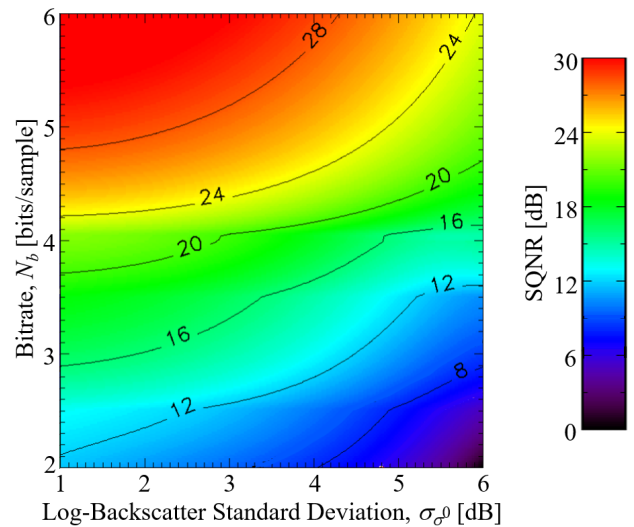


Fig. 3. SQNR as function of standard deviation of the log-backscatter σ_{σ^0} and of the bitrate N_b . The contours are obtained by interpolation of the SQNR values given in Fig. 2.

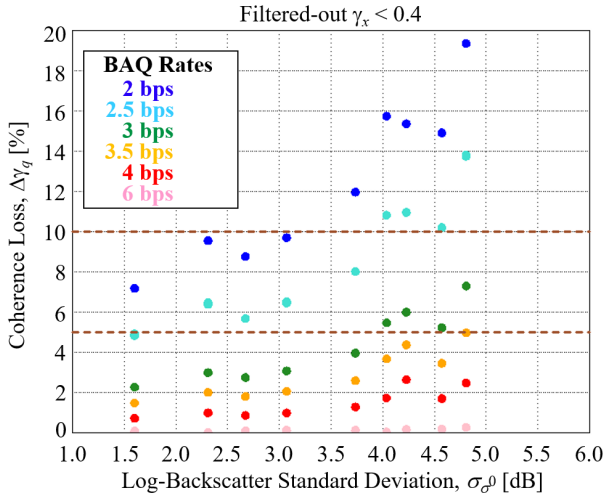


Fig. 4. Mean coherence loss $\Delta\gamma_q$ as a function of σ_{σ^0} for different bitrates. The two horizontal brown lines trace exemplary requirements on coherence loss of 5% and 10%, which are considered in Section IV for the assessment of the proposed PO-BAQ. For the derivation of σ_{σ^0} and of the mean $\Delta\gamma_q$, pixels with $\gamma_x < 0.4$ are filtered out.

1) *Signal-to-Quantization Noise Error*: Fig. 1 shows a zoom-in of the radar backscatter σ^0 for the test site over (a) the agricultural area in Iowa (USA) and (b) the urban area of Mexico City. The former (Fig. 1(a)) extends by about 3 km \times 8 km in azimuth and range, respectively, it is characterized by flat terrain and a rather homogeneous backscatter area ($\sigma_{\sigma^0} \approx 2$ dB), resulting in a mean SQNR of about 15 dB for the 3-bit BAQ case (Fig. 1(c) and Fig. 1(e)); the latter (Fig. 1(b)) extends by about 4 km \times 8 km in azimuth and range, respectively, and it shows heterogeneous backscatter due to the presence of urban settlements as well as of rugged terrain (and $\sigma_{\sigma^0} \approx 4.5$ dB), for which smaller SQNR values are observed in Fig. 1(d) and Fig. 1(f). In particular, higher SQNR values are observed in correspondence of high backscatter areas, and vice versa, as a consequence of the low-scatterer suppression effect, recalled in Section II-A. The main acquisition parameters for the two SAR scenes shown in Fig. 1 are listed in Table III.

We have repeated this analysis for all available test areas and Fig. 2 shows the mean SQNR (derived as in (8)), as a function of the standard deviation of the SAR backscatter σ_{σ^0} for different quantization rates. Each dot represents the value obtained for a single SAR acquisition and bitrate. The test areas are summarized in Table II and have a typical extension of 30 km in ground range and between 25 km and 50 km in azimuth. In addition, due to the described masking effect, low-SNR areas are significantly affected by quantization errors. However, these show in general bad performance (SNR, coherence) and therefore the impact of quantization on the overall performance is limited [44]. For this reason, areas with total coherence (prior to quantization) $\gamma_x < 0.4$ have not been included for performance assessment as well as for the derivation of the backscatter statistics σ_{σ^0} .

Looking at Fig. 2, σ_{σ^0} and the resulting SQNR are indeed correlated and, as expected, lower SQNR values are obtained

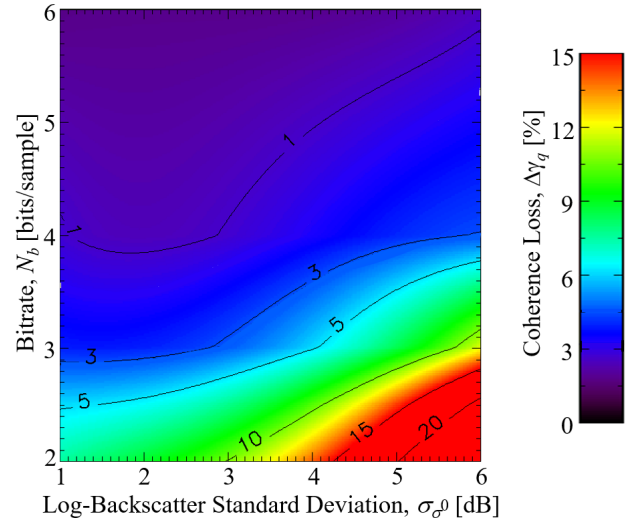


Fig. 5. Coherence loss as function of log-backscatter standard deviation σ_{σ^0} and of the bitrate N_b . The contours are obtained by interpolating the coherence loss values given in Fig. 4.

for heterogeneous regions, such as urban areas or mountainous terrain, which is consistent with the results shown in Fig. 1. The two horizontal brown lines trace exemplary requirements of SQNR = 15 dB and SQNR = 20 dB, from which the minimum required BAQ rate can be retrieved. As an example, to achieve an SQNR of 15 dB over homogeneous forest, snow/ice, or agricultural about 3 bits/sample are required (green dots), while to achieve the same performance over, e.g., urban areas about one bit more is required (red dots, corresponding to 4 bits/sample). By properly interpolating the information shown in Fig. 2, one obtains the look-up table shown in Fig. 3 which provides the expected SQNR for any value of σ_{σ^0} (ranging between 1 dB and 6 dB) and available bitrates N_b (2-bit to 6-bit BAQ).

2) *Coherence Loss*: Fig. 4 shows the mean coherence loss $\Delta\gamma_q$ (derived as in (9)), as a function of the standard deviation of the SAR backscatter σ_{σ^0} for different quantization rates. As done for Fig. 2, the results shown in Fig. 4 are obtained by filtering out pixels characterized by total coherence $\gamma_x < 0.4$ (both for the estimation of σ_{σ^0} and of $\Delta\gamma_q$) in order to exclude low SAR performance areas. The SAR intensity has been multi-looked at a final posting of 12 m \times 12 m in azimuth and ground range, respectively, while for the InSAR coherence estimation a square window of 11 \times 11 pixels is used, hence leading to a number of looks $N_1 > 100$. In the Appendix of this paper we investigate the influence of SAR backscatter inhomogeneities on the estimation accuracy of the interferometric coherence, as this may have an impact on the statistics obtained in Fig. 4 and, in turn, on the resulting performance-optimized bitrate determination. A significant increase in the coherence bias and standard deviation is observed for a “strong” texture scenarios w.r.t. a “moderate” texture and a homogeneous case especially for low-coherence signals: image texture, simulated with a short wave period w.r.t. the coherence estimation window, in combination with large backscatter heterogeneity causes samples from different

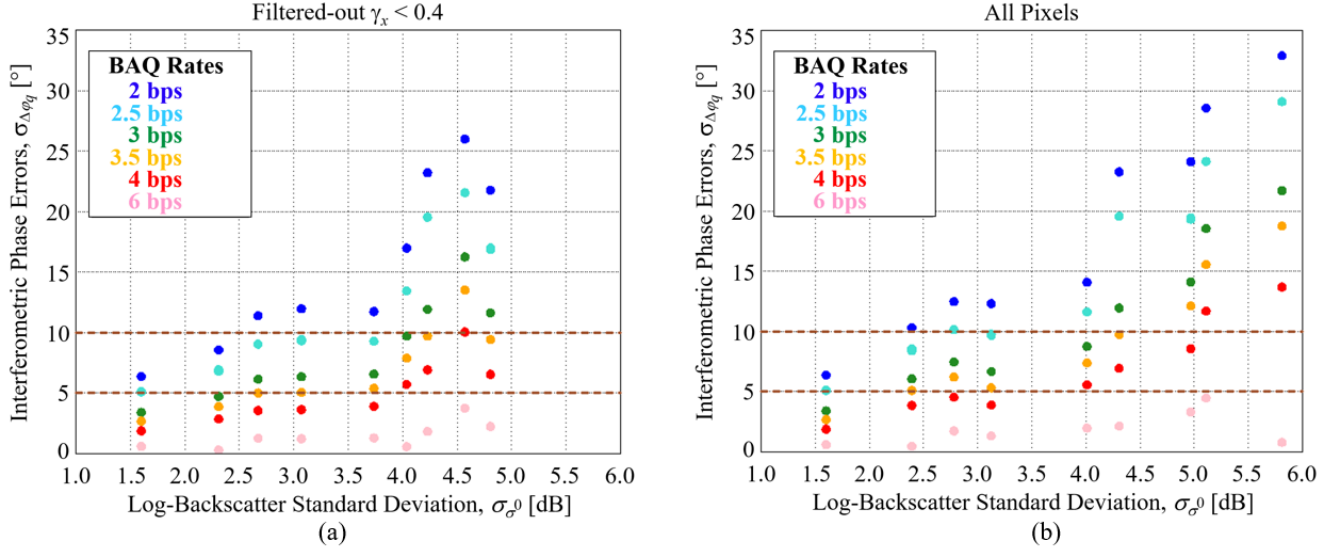


Fig. 6. Standard deviation of the interferometric phase error $\sigma_{\Delta\varphi_q}$ (derived as in (11)) as a function of the radar backscatter standard deviation σ_{σ^0} for different BAQ rate configurations. Each value of σ_{σ^0} corresponds to a different test site, as listed in Table II. (a) For the derivation of σ_{σ^0} and of the mean $\sigma_{\Delta\varphi_q}$, pixels with $\gamma_x < 0.4$ are filtered out. (b) For the derivation of σ_{σ^0} and of $\sigma_{\Delta\varphi_q}$, all image pixels are considered. The two horizontal brown lines trace exemplary phase error requirements of 5° and 10° , from which the bitrate to be used for a certain SAR scene can be derived.

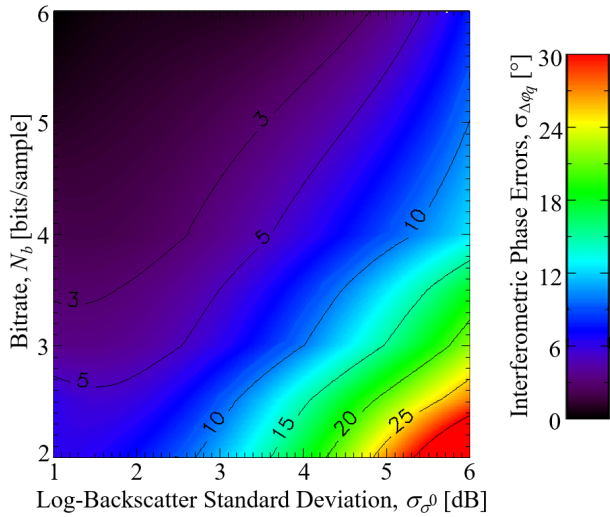


Fig. 7. Standard deviation of the interferometric phase errors $\sigma_{\Delta\varphi_q}$ as function of the log-backscatter standard deviation σ_{σ^0} and of bitrate N_b . The contours are obtained from an interpolation of the phase error values given in Fig. 6(a).

populations to be mixed with each other, resulting in a significant bias/dispersion in the coherence estimate. This aspect needs to be carefully taken into account for performance prediction and assessment, especially over low-coherence areas and when a limited number of looks $N_1 < 20$ is used for coherence estimation. On the other hand, one has to point out that, for the TanDEM-X mission case, given the larger window size used for coherence estimation (typically $N_1 > 100$), the increase in terms of coherence bias over inhomogeneous areas w.r.t. the homogeneous case is expected to be rather small even over low-coherence textural areas, as demonstrated in

Fig. 29. In addition, the coherence loss due to quantization $\Delta\gamma_q$ depicted in Fig. 4 is computed as a coherence ratio (uncompressed vs BAQ compressed coherence). Therefore, possible inaccuracies in the coherence estimation are partially compensated in its derivation, which ultimately leads to a negligible variation in the bitrate determination according to the proposed performance-dependent bit allocation.

The resulting $\Delta\gamma_q$ is strongly correlated with the dispersion of the radar backscatter σ_{σ^0} and, as expected, lower values of coherence loss (up to 10%) are obtained for homogeneous regions ($\sigma_{\sigma^0} < 3$ dB), while $\Delta\gamma_q$ values up to 20% are observed over rugged terrain and urban areas. The two horizontal brown lines trace exemplary requirements of $\Delta\gamma_q = 5\%$ dB and $\Delta\gamma_q = 10\%$, from which the minimum required BAQ rate can be defined: as an example, about 2.5 bits/sample (turquoise dots) are required to achieve a 5% coherence loss over rather homogeneous areas, while, in order to fulfill the same performance over urban/rugged terrain, about one bit more (orange dots, corresponding to 3.5 bits/sample) is required. By interpolating the information shown in Fig. 4, one obtains the look-up table in Fig. 5 which provides the expected coherence loss for any pair of $\sigma_{\sigma^0}^0/N_b$ values ranging between 1 dB and 6 dB, as well as 2 bits/sample and 6 bits/sample, respectively.

3) *Interferometric Phase Errors*: The same analysis has been conducted to assess the effects of quantization on interferometric phase errors $\Delta\varphi_q$, estimated as in (11). Fig. 6 shows the standard deviation of the phase errors $\sigma_{\Delta\varphi_q}$, as a function of σ_{σ^0} for different quantization rates. The results shown in Fig. 6(a) are obtained by filtering out pixels showing a total coherence $\gamma_x < 0.4$. For comparison, in Fig. 6(b) all pixels have been included for the estimation of $\sigma_{\Delta\varphi_q}$ and of σ_{σ^0} , and one can notice the significant increase of

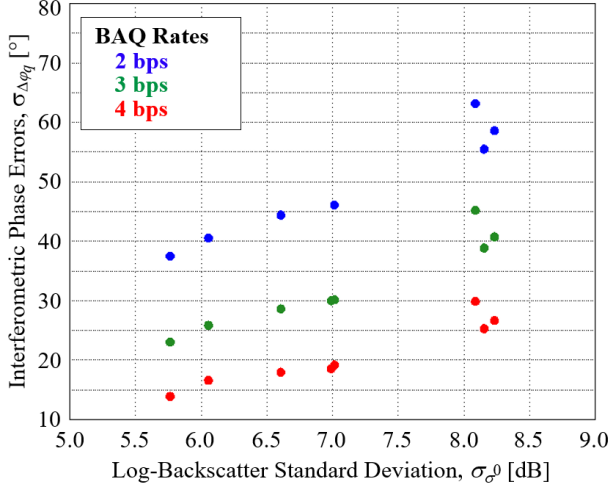


Fig. 8. Standard deviation of the interferometric phase error $\sigma_{\Delta\varphi_q}$ (derived as in (11)) as a function of the radar backscatter standard deviation σ_{σ^0} for full-resolution (i.e. single-look, $N_1=1$) data for representative test sites and BAQ rate configurations.

σ_{σ^0} as well as of the resulting phase error $\sigma_{\Delta\varphi_q}$, as a consequence of the inclusion of low-coherence areas, which are particularly affected by quantization errors. The SAR intensity as well as the InSAR phase matrices have been multi-looked to an interferometric posting $\Delta p = 12$ m, which, given the typical azimuth and range resolution of TanDEM-X, leads to number of looks N_1 ranging between 14 and 30. The resulting $\sigma_{\Delta\varphi_q}$ and σ_{σ^0} are highly correlated and, as expected, lower phase error values (up to about 13°) are observed for homogeneous regions ($\sigma_{\sigma^0} < 3$ dB), while $\sigma_{\Delta\varphi_q}$ values up to 25° for the “filtered” data (Fig. 6(a)) and up to 30° - 35° for the “unfiltered” data (Fig. 6(b)) are observed over rugged terrain and urban areas. The two horizontal brown lines trace exemplary requirements of $\sigma_{\Delta\varphi_q} = 5^\circ$ and $\sigma_{\Delta\varphi_q} = 10^\circ$, from which the minimum required BAQ rate can be defined: as an example looking at Fig. 6(a), about 2.5-3 bits/sample (turquoise dots) are required to achieve a 5° phase error over homogeneous areas, while about 4-5 bits/sample are required to fulfill the same performance over urban/rugged terrain areas. By interpolating the information shown in Fig. 6(a), we derived the contour plot in Fig. 7 which provides the expected $\sigma_{\Delta\varphi_q}$ for any pair of σ_{σ^0} (ranging between 1 dB and 6 dB) and N_b from 2 bits/sample up to 6 bits/sample.

In addition to the quantization rate N_b and the standard deviation of the SAR backscatter distribution σ_{σ^0} , which have been considered in the present investigations, the number of interferometric looks N_1 also impacts the resulting quantization errors. It has already been mentioned that the SAR intensity as well as the interferometric phase errors have been estimated after proper multi-looked of the full-resolution data at a final posting of $12 \text{ m} \times 12 \text{ m}$ in azimuth and ground range. For comparison, we have evaluated the InSAR phase errors due to quantization on full-resolution data (i.e. $N_1=1$ look), which are shown in Fig. 8 as a function of the standard deviation of the SAR backscatter σ_{σ^0} , for representative

BAQ rates and test sites. For what concerns the statistics of the SAR backscatter σ_{σ^0} , its values are, for the single-look scenes, 3.5 dB to about 4 dB larger than those obtained with multi-looked data at 12 m posting, as it can be observed by comparing them with the values shown in Fig. 6(b). Regarding the interferometric phase error, one can verify once again that the quantization errors increase for areas showing larger heterogeneity in the SAR backscatter. In particular, by comparing the phase error values in Fig. 8 with those obtained for the 12-m posting data of Fig. 6(b), one can observe a test-site dependent increase of a factor ρ due to the reduction of looks:

- $\rho \in [6, 7]$ for the very homogeneous area in the Greenland ice sheet (e.g., for 3-bit, $\sigma_{\Delta\varphi_q} = 23^\circ$ for single-look, $\sigma_{\Delta\varphi_q} = 3.4^\circ$ for 12-m posting data),
- $\rho \sim 4$ for the homogeneous agricultural area in Iowa (for 3-bit BAQ, $\sigma_{\Delta\varphi_q} = 25.8^\circ$ for single-look, $\sigma_{\Delta\varphi_q} = 6^\circ$ for 12-m posting data),
- $\rho \sim 3.5$ for the rocky area in Death Valley (for the 3-bit case, $\sigma_{\Delta\varphi_q} = 30.1^\circ$ for single-look, $\sigma_{\Delta\varphi_q} = 8.7^\circ$ for 12-m posting data),
- $\rho \sim 2$ for the mountainous forested area in Malaysia (for the 3-bit case, $\sigma_{\Delta\varphi_q} = 38.8^\circ$ for single-look, $\sigma_{\Delta\varphi_q} = 18.5^\circ$ for 12-m posting data).

It is worth pointing out that the mentioned increase in terms of backscatter standard variation ($\Delta\sigma_{\sigma^0} = 3.5$ -4 dB) as well as of phase errors ($\rho \in [6, 7]$) observed for the single-look SAR products with respect to the multi-looked ones, is in good agreement with that obtained by simulating an artificial and homogeneous scene modeled by complex Gaussian noise and Rayleigh amplitude statistics. On the other hand, such a significant variation in terms of phase error increase ρ , as function of interferometric looks with respect to the local backscatter statistics, can be interpreted as a consequence of the highly non-linear nature of the distortion induced by the SAR raw data quantization.

Finally, in the context of a SAR mission scenario, it is of interest to consider the number of data takes N_{acq} acquired over a certain location on Earth, i.e., the dimension of the image stack for the specific SAR application. N_{acq} depends on the available resources, such as the onboard memory, the downlink capacity, as well as the mission lifetime, and can be interpreted as a sort of “temporal” looks, hence contributing to mitigate the resulting phase error due to quantization in the same way as done in the spatial domain by N_1 .

IV. PERFORMANCE-OPTIMIZED BLOCK-ADAPTIVE QUANTIZATION (PO-BAQ)

The results shown in the previous section are exploited to implement the proposed performance-optimized block-adaptive quantization (PO-BAQ) which allows one to control the compression rate and, at the same time, the resulting performance degradation. According to that, the required bitrate $N_{b,\text{req}}$ to be used for SAR raw data quantization is determined as a function of the considered parameters

$$N_{b,\text{req}} = f(\zeta_{\text{req}}, \sigma_{\sigma^0}, N_1, N_{\text{acq}}). \quad (13)$$

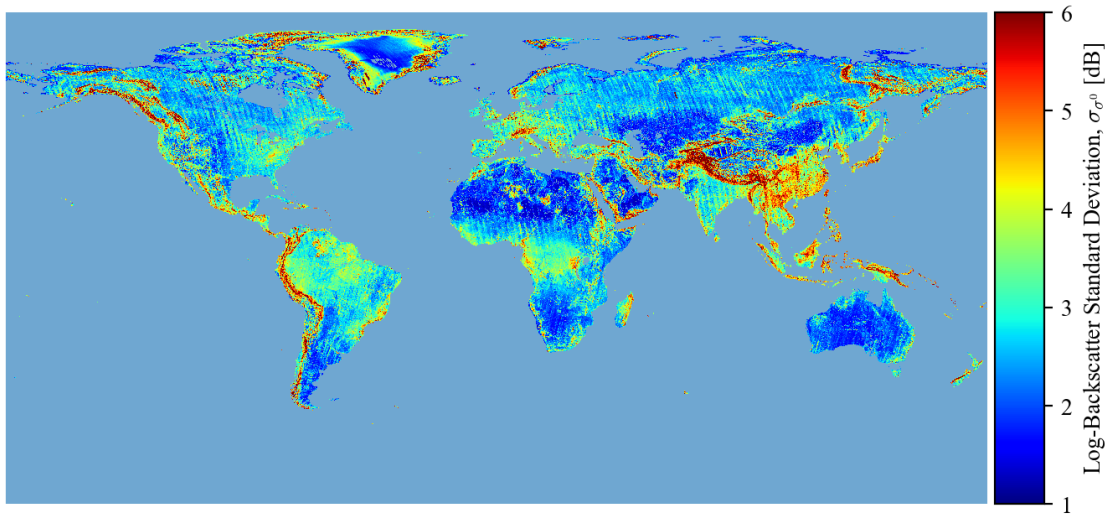


Fig. 9. Global X-band backscatter standard deviation map derived from the first global acquisition of TanDEM-X [51], which is exploited in this paper to derive global bitrate maps according to the proposed performance-optimized quantization method.

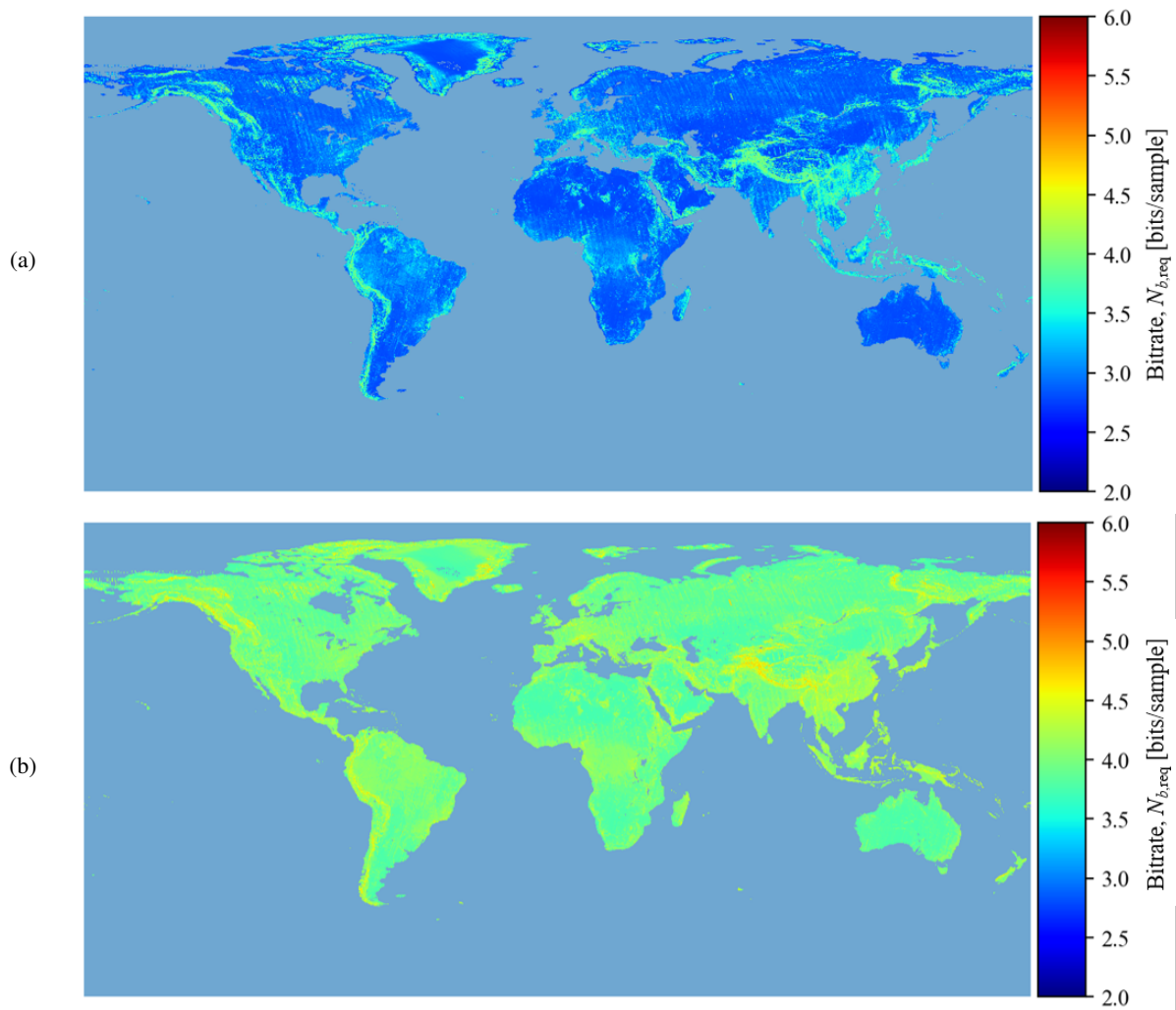


Fig. 10. Global bitrate maps resulting from a requirement of (a) SQNR = 15 dB and (b) SQNR = 20 dB.

In the above equation, ζ_{req} represents the requirement imposed on the parameter ζ , which can be defined in terms of, e.g., SQNR, coherence loss, or interferometric phase error; σ_{σ^0} is

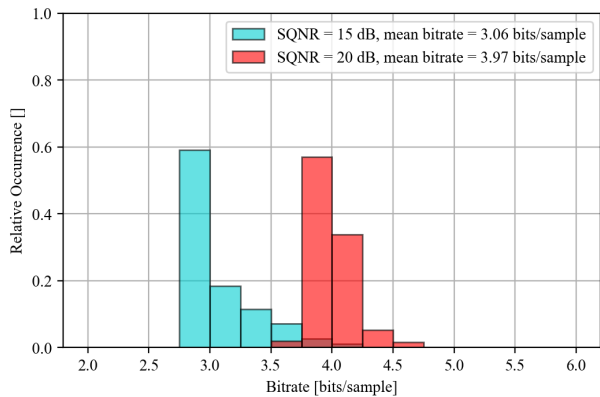


Fig. 11. Bitrate distribution for SQNR requirements. The turquoise bins indicate the distribution of the bitrate map shown in Fig. 10(a) (SQNR = 15 dB), while the red bins represent the bitrate map in Fig. 10(b) (SQNR = 20 dB).

the local backscatter information, which has to be available as external input (i.e. a priori) before data take commanding; if the requirement is set on the interferometric phase errors $\sigma_{\Delta\varphi_q}$, the number of looks N_1 (determined by the system resolution and the target posting) and the number of available acquisitions N_{acq} (defined at mission planning) must be included in the optimization as well, as described in Section III-B3. The function $f(\cdot)$ in (13) is defined by the information provided in Fig. 3, Fig. 5, or Fig. 7, which can be regarded as a sort of look-up-table (LUT) that provides the expected degradation for the corresponding performance parameter as a function of the bitrate N_b and of the backscatter statistics σ_{σ^0} . According to the proposed PO-BAQ, once ζ_{req} , N_1 , and N_{acq} are fixed, and the standard deviation of the SAR backscatter scene to be acquired σ_{σ^0} is known a priori (obtained from an external source), the required number of bits $N_{b,\text{req}}$ is derived as

$$N_{b,\text{req}} = \arg \max_{N_b \in [N_{b,\text{min}}, N_{b,\text{max}}]} \left\{ \zeta(N_b, N_1, N_{\text{acq}}, \sigma_{\sigma^0}) \leq \zeta_{\text{req}} \right\} \quad (14)$$

being $N_{b,\text{min}}$ and $N_{b,\text{max}}$ the minimum and maximum allowed bitrates, respectively, which are typically determined at system/instrument design. The proposed method has been evaluated by exploiting as input a global X-band backscatter variance map derived from the first DEM acquisition of TanDEM-X, as presented in [51], which is shown in Fig. 9. The images are mosaicked at a final resolution of $5 \text{ km} \times 5 \text{ km}$ at the equator, which corresponds to an angular spacing of 0.05° in latitude/longitude coordinates. The backscatter standard deviation σ_{σ^0} is evaluated as the sample standard deviation of the available values inside the considered output cell [51]. Consistently with the results observed so far, in the figure one can notice low values of σ_{σ^0} , typically below 2 dB in correspondence of, e.g., the flat rocky deserts in Australia and South Africa, or the Sahara desert, as well as the central region in Greenland, characterized by homogeneous snow and ice cover. On the other hand, larger σ_{σ^0} values up to 6-7 dB are obtained over hilly and rugged terrain, such as the Himalayas, the Alps, the Andes, or the tropical forest in Indonesia. The combined information has been exploited

for the generation of global bitrate maps, which provide the required quantization rates $N_{b,\text{req}}$ to be used in order to fulfill the specification as in (14), which is presented in the following.

A. PO-BAQ for Global Mapping Applications

Fig. 10(a) and Fig. 10(b) show the global bitrate maps resulting from a requirement on the SQNR of 15 dB and 20 dB, respectively, which have been derived by exploiting the LUT in Fig. 3. Looking at Fig. 10(a), lower bitrates of about 3 bits/sample (represented by the bluish areas) are needed in correspondence of homogeneous areas, such as flat sandy (e.g. Sahara) and rocky (e.g. Australia) deserts, as well as the central region in Greenland, or the Eurasian Steppe. On the other hand, about one bit more is required over hilly and rugged terrain, such as the Andean Mountains, the Himalayas, or the tropical forest in Indonesia. Similar considerations can be made for the map depicted in Fig. 10(b), where the required bitrate typically ranges between 4 bits/sample and 5 bits/sample. The corresponding bitrate distribution is provided in Fig. 11 for the SQNR requirement of 15 dB (turquoise) and 20 dB (red). In addition, Fig. 12(a) and Fig. 12(b) show an estimate of the global SQNR map if a constant 3-bit and 4-bit BAQ is used, respectively. Here, low SQNR values over mountainous regions as well as higher values over flat and homogeneous regions can be consistently observed. Fig. 13 shows the global distribution of SQNR for the 3-bit (turquoise bins) and 4-bit (red) BAQ, and the average SQNR values are of about 15 dB and 20 dB, which is consistent with the results in Fig. 11 and the theoretical performance [4], [52].

Fig. 14(a) shows the global bitrate maps resulting from a coherence loss requirement of $\Delta\gamma_q = 5\%$, while Fig. 14(b) depicts the bitrate if a requirement of $\Delta\gamma_q = 10\%$ is imposed. Both maps are derived by combining the global map of backscatter standard deviation [51] and the LUT in Fig. 5. Similar conclusions can be drawn as done for Fig. 10(a) and Fig. 10(b) (please note the different bitrate range used in the maps from 2 to 4 bits/sample). The corresponding bitrate distribution is given in Fig. 15 for the $\Delta\gamma_q$ requirement of 5% (turquoise bins) and 10% (red). Fig. 16(a) depicts a global map of the expected coherence loss in case a constant 3-bit BAQ is used, and $\Delta\gamma_q$ values of about 3-4% are observed over homogeneous terrain, while up to 8-10% coherence loss is observed over mountainous regions. Similarly, Fig. 16(b) shows the global coherence loss for the 4-bit BAQ case, and small $\Delta\gamma_q$ values of about 1% and up to 4% are observed over homogeneous areas and heterogeneous regions, respectively. Fig. 17 shows the corresponding distribution of $\Delta\gamma_q$ for the 3-bit BAQ (turquoise) and 4-bit (red) case, and the obtained average values are consistent with the expected performance [4], [44].

Finally, Fig. 18(a) and Fig. 18(b) show the global bitrate maps resulting from a requirement on the interferometric phase error of $\sigma_{\Delta\varphi_q} = 5^\circ$ and $\sigma_{\Delta\varphi_q} = 10^\circ$, respectively, obtained by combining the X-band backscatter standard deviation map in [51] with the information derived in Fig. 7. For the 5° requirement (Fig. 18(a)) a larger dispersion in terms

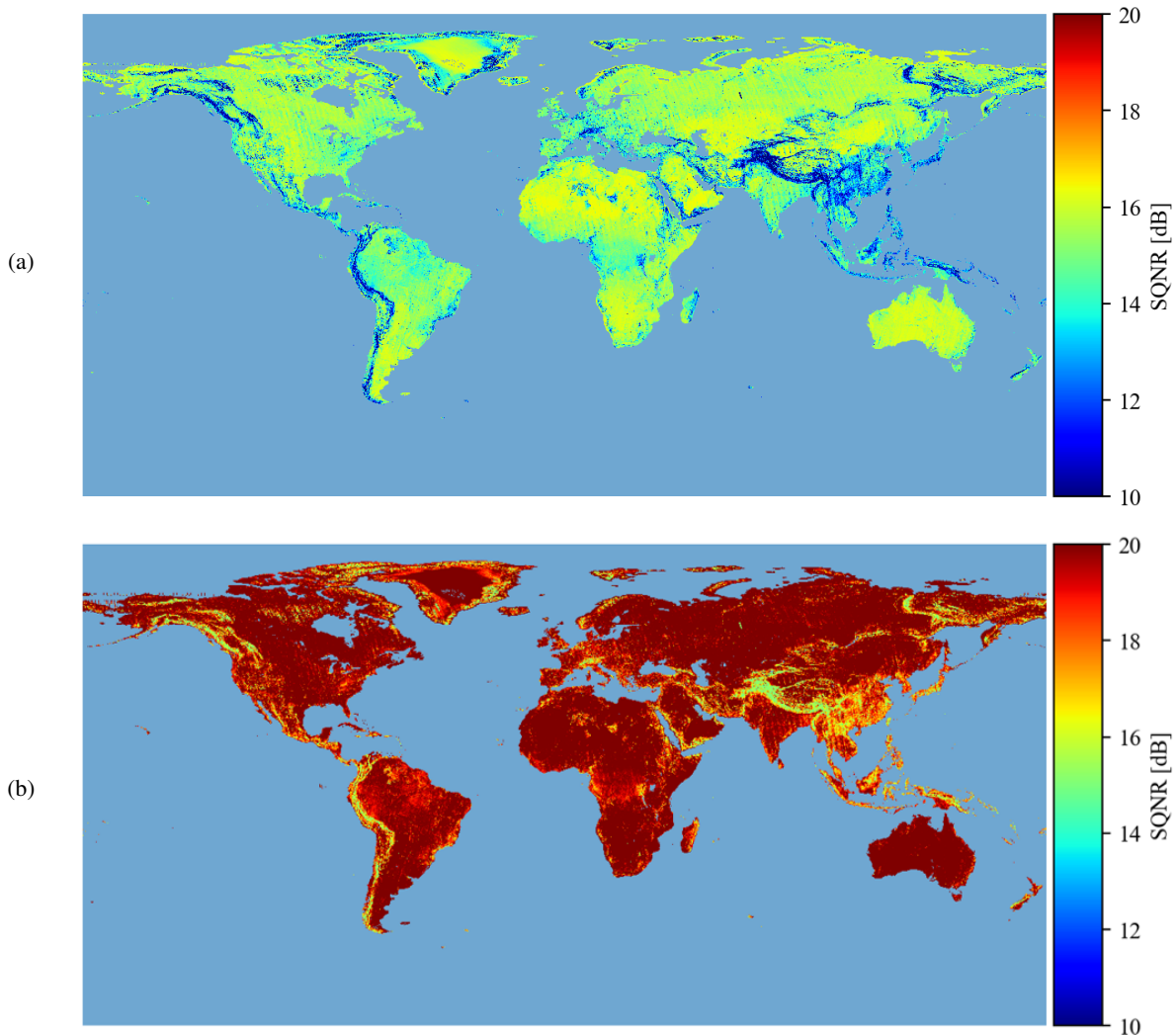


Fig. 12. Global SQNR map resulting from a fixed BAQ rate of (a) 3 bits/sample and (b) 4 bits/sample.

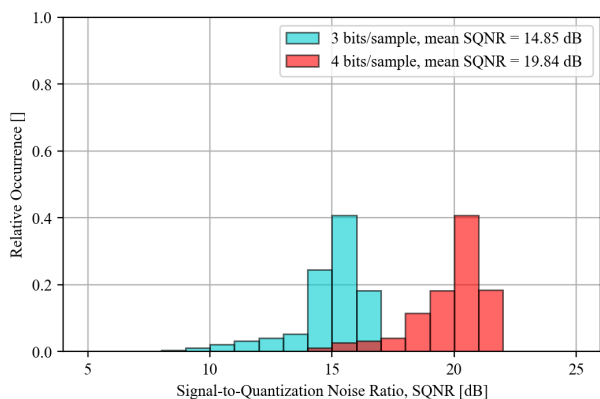


Fig. 13. SQNR distribution for fixed BAQ rates. The turquoise bins indicate the distribution of the SQNR map for 3-bit BAQ (shown in Fig. 12(a)), while the red bins represent the SQNR distribution for 4-bit BAQ (shown in Fig. 12(b)).

of required bitrate values can be noticed, ranging between 2.5 bits/sample and 6 bits/sample, as it can be seen also in Fig. 19 (turquoise bins), while for the 10° requirement

(Fig. 18(b) and red bins in Fig. 19) most of the areas would require a minimum bitrate of 2-bit BAQ, thanks to the more relaxed constraint. Fig. 20(a) and Fig. 20(b) depict the global map of the InSAR phase error for a 3-bit and 4-bit BAQ case, respectively, and Fig. 21 shows the corresponding distributions of $\sigma_{\Delta\varphi_q}$. For the 3-bit BAQ (turquoise bins) an average error of about 6° is obtained, while the use of 4 bit/sample (red) results in an average $\sigma_{\Delta\varphi_q}$ between 3° and 4° , even though both histograms are rather dispersed in the range between 2° (over homogeneous regions) and 15° (required over rugged terrain and urban areas).

B. Applications at Sub-Scene Scale

We now investigate the opportunity of refining the performance optimization and bitrate allocation at sub-scene level, as introduced in [53]. Since the responses of the scatterers under illumination overlap in the raw data domain within an area A_{SAR} as defined in (2), the use of a given bitrate N_b applied to a portion of the raw data matrix affects the performance, in the focused image, also in areas located in close vicinity. This principle is represented by the red arrows

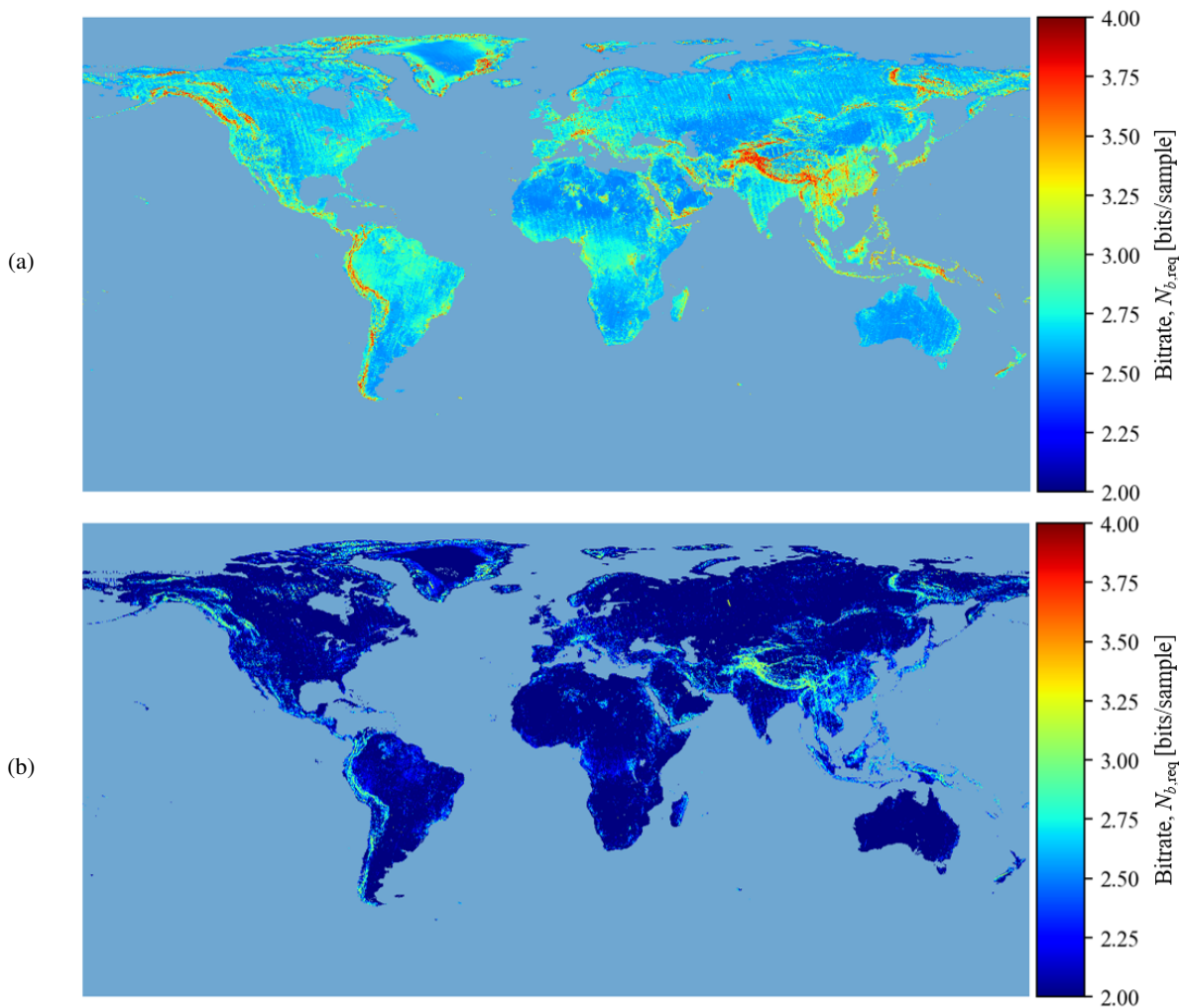


Fig. 14. Global bitrate map resulting from a requirement on the coherence loss of (a) $\Delta\gamma_q = 5\%$ and (b) $\Delta\gamma_q = 10\%$.

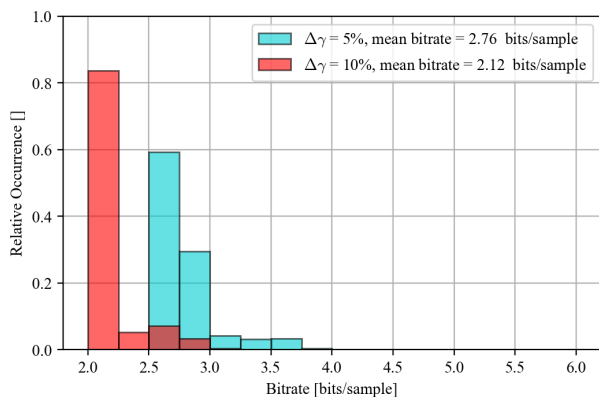


Fig. 15. Bitrate distribution resulting from requirements on coherence loss $\Delta\gamma_q$. The turquoise bins indicate the distribution of the bitrate map shown in Fig. 14(a) ($\Delta\gamma_q = 5\%$), while the red bins represent the bitrate map in Fig. 14(b) ($\Delta\gamma_q = 10\%$).

in Fig. 22. In turn, the performance of the central block is impacted by the bitrates used for quantizing the raw data located within the same area A_{SAR} , an effect which is sketched by the blue arrows in Fig. 22 (for TanDEM-X, the synthetic

aperture L_s and the chirp length L_{chirp} are in the order of a few kilometers). In the same figure, the green segment d_{step} indicates the step length, which is assumed, for the sake of simplicity, to be the same in azimuth and range, used for sliding the SAR image block at each PO-BAQ iteration, which also defines the final “pixel size” of the resulting bitrate map. All that considered, we applied the proposed method to the SAR backscatter map σ^0 acquired by TanDEM-X over the “Death Valley” (USA) test site of Table II, which is depicted in Fig. 23(a). The region extends by about 35 km in azimuth and ground range, and is characterized by the presence of non-vegetated, rocky mountains. The main acquisition parameters for the SAR scene investigated in this analysis are listed in Table IV. Fig. 24 shows the phase error $\sigma_{\Delta\varphi_q}$ evaluated for each SAR image block of size A_{SAR} and different quantization rates, and a strong correlation between backscatter heterogeneity and phase error can be once again verified (the σ_{σ^0} values are different from those shown, e.g., in Fig. 6, as for Fig. 24 the backscatter statistics are calculated on full-resolution data of about $3 \text{ m} \times 3 \text{ m}$, i.e., no multi-looking is applied). The procedure for bitrate determination described in the first part of this section is repeated for each SAR

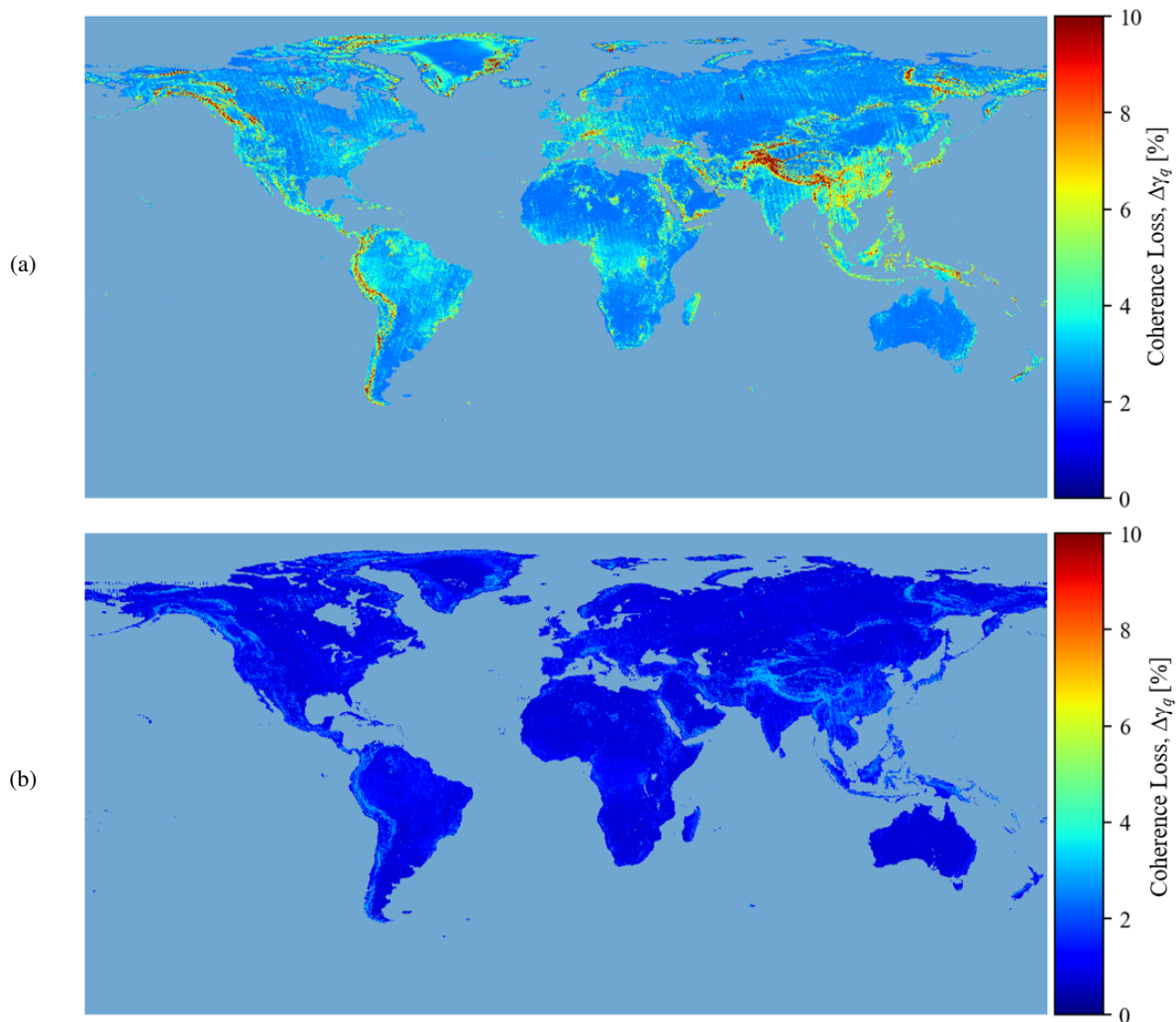


Fig. 16. Global map of coherence loss due to quantization $\Delta\gamma_q$ map resulting from a fixed BAQ rate of (a) 3 bits/sample and (b) 4 bits/sample.

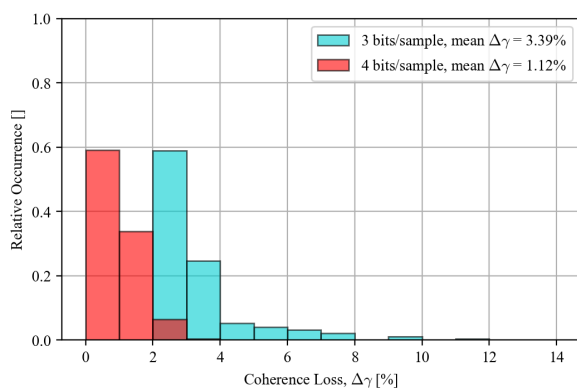


Fig. 17. Distribution of coherence loss due to quantization for fixed BAQ rates. The turquoise bins indicate the distribution resulting from 3-bit BAQ (shown in Fig. 16(a)), while the red bins represent the coherence loss resulting from constant 4-bit BAQ (shown in Fig. 16(b)).

image block, so that the compression rate $N_{b,\text{req}}$ is derived by matching the standard deviation of each SAR image block of size A_{SAR} with the target requirement.

Fig. 23(b) shows the resulting bitrate map by assuming a

posting of 12 m in azimuth/ground range (leading to $N_1 = 16$ looks), $N_{\text{acq}} = 1$, and $\sigma_{\Delta\varphi_q,\text{req}} = 10^\circ$. For this example, a step length used for sliding the SAR image block at each iteration $d_{\text{step}} = 500$ (as in Fig. 22) has been set, which corresponds to the “resolution” of the corresponding bitrate map. The mixing effect of the target responses in the raw data described in Fig. 22 results in a sort of low-pass filtering in the obtained bitrate map, for which smooth transitions between different values of N_b are typically observed with respect to the actual backscatter variability. As expected, larger values of $N_{b,\text{req}}$, up to 5 bits/sample, are obtained in correspondence of the pronounced topography (lower right part of Fig. 23(a)), with respect to the more homogeneous region in the upper half of the image, for which smaller BAQ rates, down to 2 bits/sample, are sufficient to fulfill the phase error requirement. Fig. 25(a) depicts the phase error map resulting from the bitrate in Fig. 23(b). Each pixel represents the standard deviation of the phase error due to quantization $\sigma_{\Delta\varphi_q}$, calculated in the data block of area A_{SAR} and centered in the corresponding pixel. About 8% of the pixels do not fulfill the requirement of $\sigma_{\Delta\varphi_q,\text{req}} = 10^\circ$, which are highlighted in dark red in the mask in Fig. 25(b).

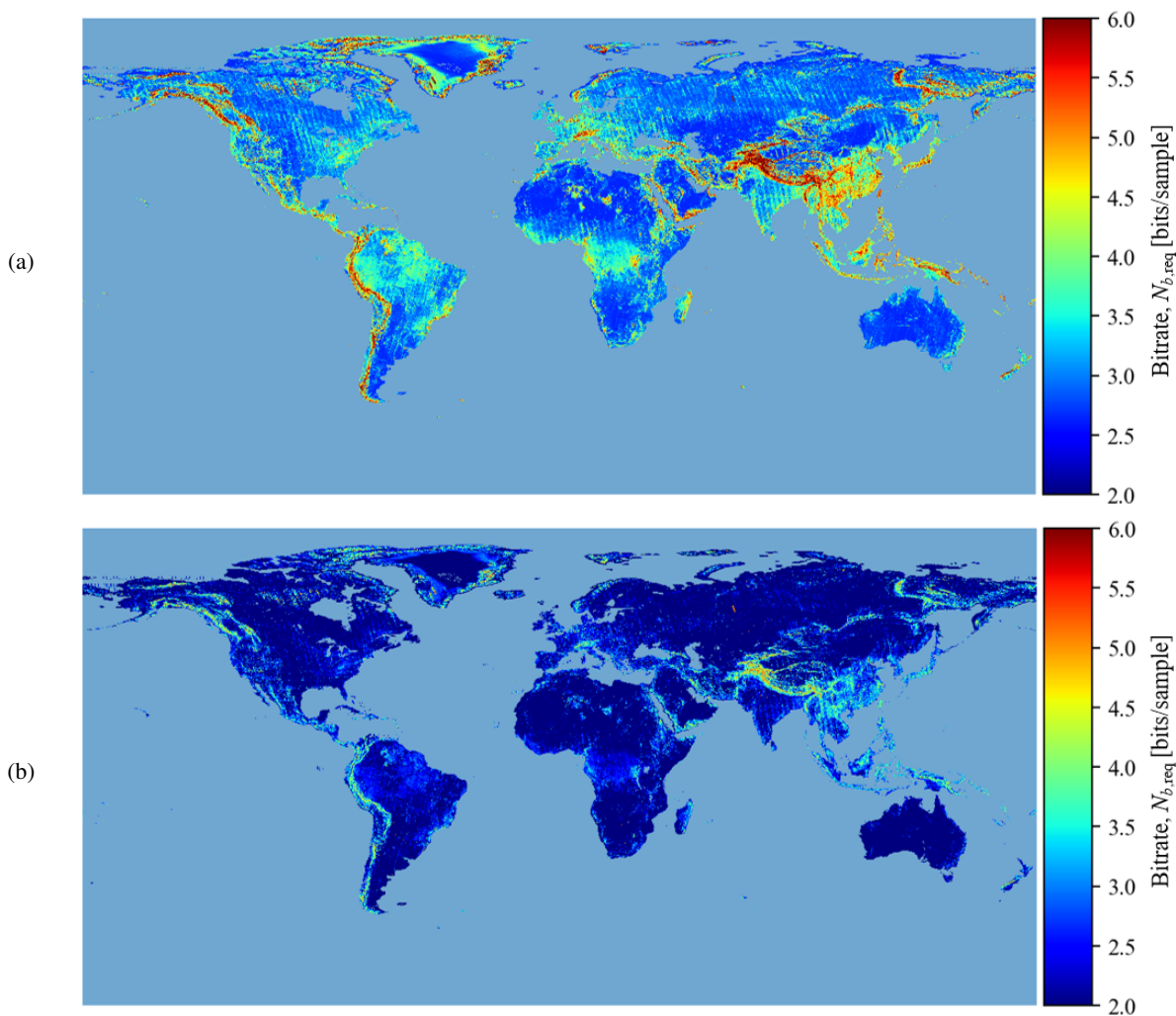


Fig. 18. Global bitrate map resulting from a phase error requirement (a) $\sigma_{\Delta\varphi_q} = 5^\circ$ and (b) $\sigma_{\Delta\varphi_q} = 10^\circ$.

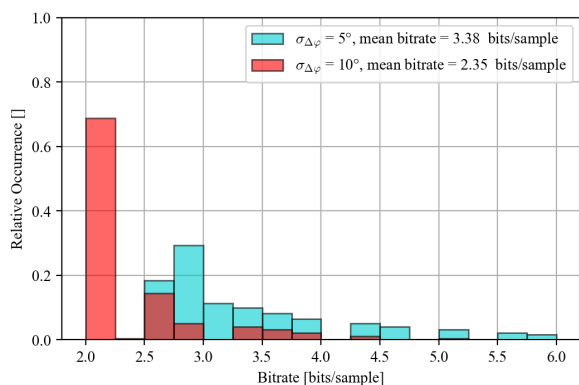


Fig. 19. Bitrate distribution resulting from requirements on phase error $\sigma_{\Delta\varphi_q}$. The turquoise bins indicate the distribution of the bitrate map shown in Fig. 18(a) ($\sigma_{\Delta\varphi_q} = 5^\circ$), while the red bins represent the bitrate map in Fig. 18(b) ($\sigma_{\Delta\varphi_q} = 10^\circ$).

This can be explained with the above-mentioned mixing effect of the target responses and resulting quantization errors. The average bitrate obtained from the bitrate map in Fig. 23(b) is $\bar{N}_{b,\text{req}} = 2.99$ bits/sample. On the other hand,

also looking at the plot in 6(b) we obtained that $\bar{N}_{b,\text{req}}$ of about 2.8 bits/sample is needed to achieve a phase error standard deviation of 10° , estimated over the entire scene (no low-performance areas have been filtered out in this example). However, with the PO-BAQ, we do aim at fulfilling the same requirement, but for each of the image blocks of size A_{SAR} , which justifies the slightly larger (about 7%) average bitrate required. Given that $\bar{N}_{b,\text{req}} = 2.99$ bits/sample, it is reasonable to compare the performance of the proposed PO-BAQ with a nominal 3-bit BAQ. Fig. 25(c) shows the phase error distribution as a function of the standard deviation of the backscatter σ_{σ_0} , calculated in the corresponding SAR intensity image block. With respect to the 3-bit BAQ case (green dots), the distribution of the PO-BAQ values (in purple) appears to be horizontally “tilted” and concentrated below the dashed brown line, which identifies the 10° requirement set as input. Fig. 25(d) depicts the histograms of the phase error values for the 3-bit BAQ (green bars) and PO-BAQ (purple bars). Again, the distribution resulting from the 3-bit BAQ shows a larger dispersion mostly between 3° and 15° . On the other hand, the values obtained from the PO-BAQ are mainly concentrated between 5° and 10° (depicted in turquoise and

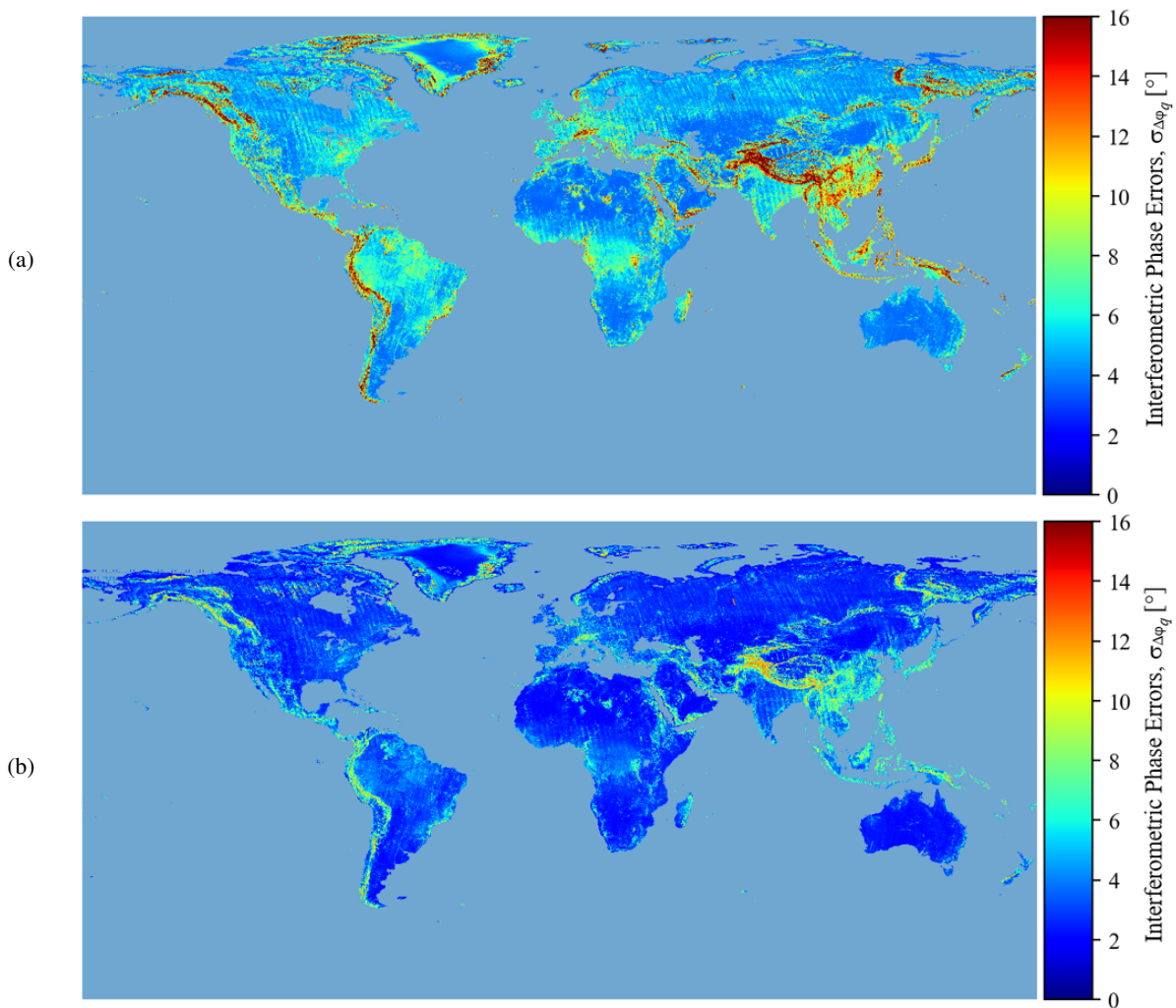


Fig. 20. Global map of phase error map due to quantization $\sigma_{\Delta\varphi_q}$ resulting from a fixed BAQ rate of (a) 3 bits/sample and (b) 4 bits/sample.

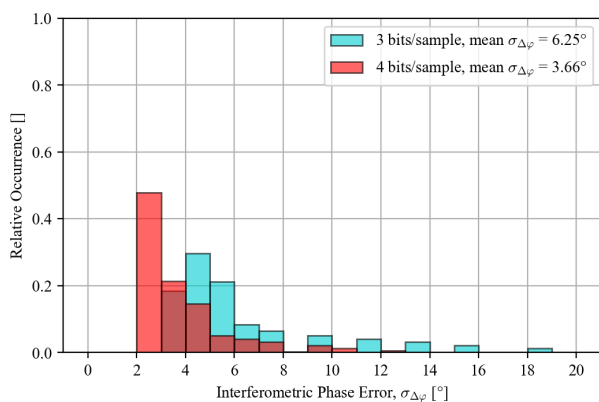


Fig. 21. Distribution of interferometric phase errors due to quantization for fixed BAQ rates. The turquoise bins indicate the distribution resulting from 3-bit BAQ (shown in Fig. 20(a)), while the red bins represent the interferometric phase errors resulting from constant 4-bit BAQ (shown in Fig. 20(b)).

yellow in Fig. 25(b)), hence demonstrating the effectiveness of the proposed method. As it has been shown in this analysis, the resulting rates are typically non-integer numbers. These can

be implemented on board by including additional hardware (e.g., a Huffman coder) prior to the quantizer block, as proposed in [20], [21]. Alternatively, although a standard BAQ scheme implements integer quantization rates only, non-integer compression rates can be effectively synthesized by toggling the integer BAQ rates along azimuth and/or range according to predefined bitrate sequences, as it is proposed in [23].

Looking at local image scale, Fig. 26 shows the SAR backscatter for the area of the Death Valley test site delimited by the red square in Fig. 23(a). In particular, the σ^0 map is depicted for the nominal 3-bit BAQ case (Fig. 26(a)) and for the proposed PO-BAQ (Fig. 26(b)) applying the bitrate map as in Fig. 23(b), and no appreciable differences can be noticed. Fig. 27 depicts the corresponding maps of the interferometric phase errors for the same area when using 3-bit BAQ (Fig. 27(a)) and the PO-BAQ (Fig. 27(b)): the difference in performance for the two cases is clearly visible as a consequence of the different compression rates applied to quantize the raw data. In this example, PO-BAQ allows therefore for a reduction of the data rate by achieving the desired phase errors performance.

It is important to highlight that, in order to implement an

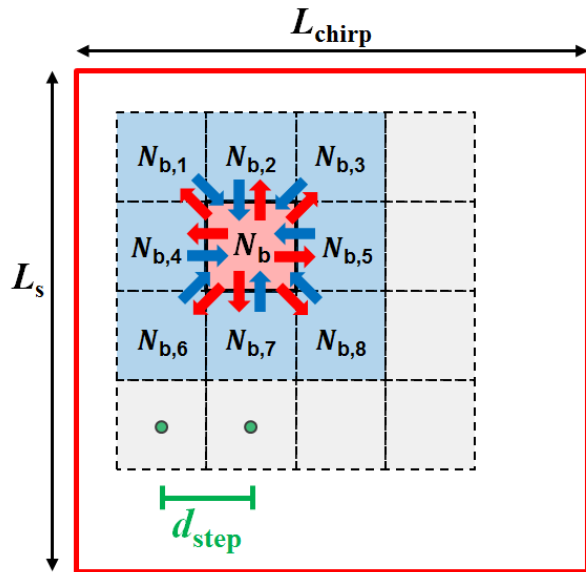


Fig. 22. The responses of the scatterers under illumination overlap in the raw data domain within an area A_{SAR} as defined in (2). The use of a given bitrate for a subset of raw data (e.g., N_b in the central block) affects the performance, in the focused data, in the areas located in close vicinity, which is ideally sketched by the red arrows. In turn, the degradation observed in the area corresponding to the red image block is affected by the bitrates used for quantizing the raw data located within the area A_{SAR} (for this, the weighting carried out by the antenna pattern in azimuth and elevation must be accounted as well). The closest blocks are indicated by $N_{b,i}$, for $i \in [1, 8]$ and the effect is represented by the blue arrows. Finally, the green segment d_{step} indicates the step length, assumed for simplicity the same in azimuth and range, which defines the pixel size of the resulting bitrate map.

optimization of performance and bitrate, PO-BAQ does not rely on any specific property of the SAR raw signal and can therefore be applied in combination with methods for data volume reduction such as those proposed in [27], [28], or [30]. For further comparison with the proposed PO-BAQ, it is also worth to recall the principle of the flexible dynamic block-adaptive quantization (FDBAQ) [21], which represents the state of the art for onboard SAR data compression and is used on the C-band Sentinel-1 SAR satellites. The FDBAQ extends the concept of block-adaptive quantization, by adaptively adjusting the quantization rate according to the local SNR [21]. Such an optimization of both performance and data rate is achieved in the raw data domain, and therefore the actual degradation in the focused SAR and InSAR products is not taken into account, which indeed represents the main advantage of the method introduced in this paper. In addition, FDBAQ exploits average backscatter statistics at C band to associate the desired bitrate to each σ^0 range. On the other hand, the implementation of the PO-BAQ relies on the a priori knowledge of accurate SAR backscatter information, down to a few kilometers scale, for the derivation of the bitrate map. Since the bitrate is determined before the data take commanding, the total required volume of data is known in advance. However, the bitrate information needs to be uplinked and implemented on the sensor, which may require additional on-board computational and processing effort. Contrarily, for the FDBAQ the data rate is estimated on board from the

statistics of the raw data samples received by the sensor during the data take, so the exact volume of data to be acquired cannot be known before commanding. This aspect complicates the mission planning in view of memory and downlink, and thereby the available downlink resources may not be fully exploited.

In this work, the performance of PO-BAQ is compared with that of BAQ operating at constant bitrate (as shown in Fig. 10 to Fig. 21), as BAQ represents the most widely used quantization standard for present SAR missions. However, we intend to carry out a comparison with FDBAQ as well, together with a more extensive benchmark of different quantization techniques, in further research activities, which will be object of future publications. In this context, it is worth to mention that FDBAQ does not foresee an optimisation on interferometric parameters (such as phase errors), and for this a consistent adaptation/development of the FDBAQ would be needed to include different quality metrics of SAR/InSAR products for a proper comparison with PO-BAQ.

V. CONCLUSIONS AND OUTLOOK

On-board raw data compression represents an aspect of utmost importance for the design of present and future SAR systems, and quantization errors in SAR data are significantly influenced by the local backscatter statistics in the SAR image. In this paper, we introduced a novel performance-optimized BAQ which grounds on state-of-the-art quantization algorithms for SAR systems and aims at optimizing the performance of the processed SAR and InSAR products. This allows for achieving a targeted bitrate allocation which can be adapted to the specific higher level SAR products and to the corresponding performance requirements. The impact of quantization on signal-to-quantization noise ratio (SQNR), coherence loss, and interferometric phase errors has been evaluated and characterized using TanDEM-X bistatic acquisitions, and the PO-BAQ has been tested on real data. We verified that the observed degradation is consistent with the expected one, demonstrating the effectiveness of the proposed method. The main advantage of the PO-BAQ with respect to the existing quantization methods is that it aims at optimizing the performance of the SAR and InSAR data products. Moreover, since the bitrate selection is defined on ground, before the data take commanding, the total required volume of data is known in advance, allowing, e.g., for a better monitoring and management of the acquisition resources. On the other hand, the bitrate map needs to be uplinked to the sensor, and the resulting bitrate selection must be properly implemented on board, which may require an additional computational effort. We intend to carry out a comparison of the proposed PO-BAQ with existing SAR quantization methods, such as the FDBAQ, in further research activities, which will be object of future publications. PO-BAQ can be opportunely combined with other data volume reduction methods, and represents a promising technique for improving the design of present and future SAR missions, since it specifically aims at a joint adaptation not only of the resource allocation but also of the product quality of the specific SAR application.

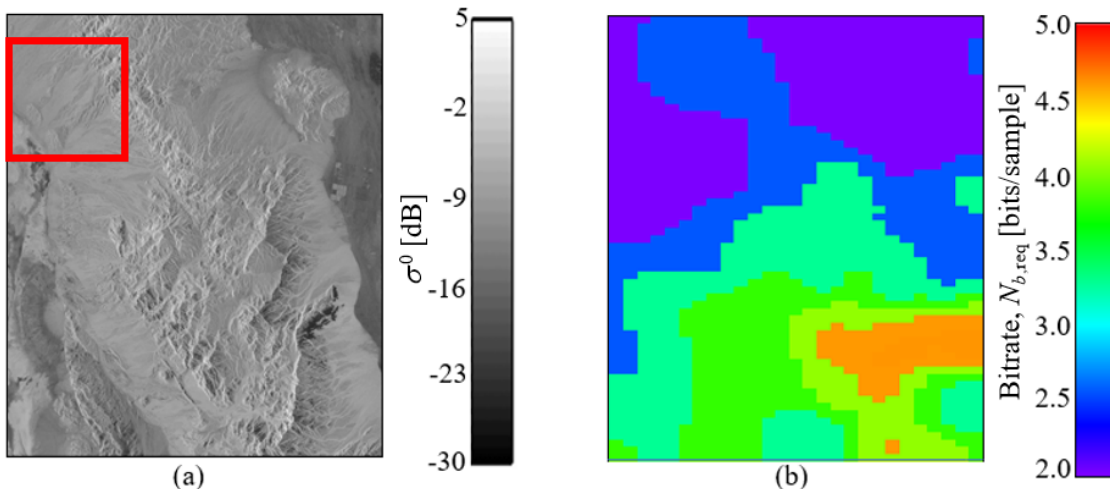


Fig. 23. (a) Radar backscatter σ^0 of the test area located in the Death Valley (USA), which extends over about 35 km both in azimuth (vertical) and range (horizontal dimension). The area delimited by the red square is further investigated in Fig. 26 and Fig. 27. (b) Bitrate map generated according to the proposed PO-BAQ ($N_{b,\text{req}}$ in (14)) for $N_l = 16$ looks, $N_{\text{acq}} = 1$, and $\sigma_{\Delta\varphi_q,\text{req}} = 10^\circ$. The average bitrate $\bar{N}_{b,\text{req}} \approx 3$ bps.

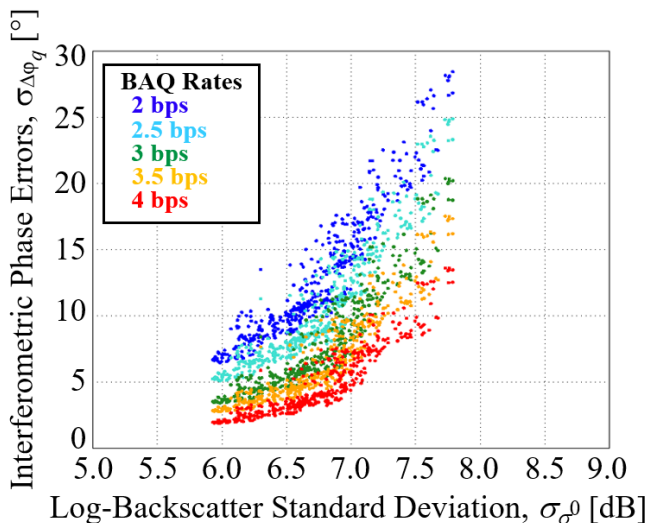


Fig. 24. Phase error standard deviation due to quantization $\sigma_{\Delta\varphi_q}$ as a function of the standard deviation of the backscatter coefficient σ_{σ^0} calculated for image blocks of area A_{SAR} of the test area located in the Death Valley (USA) for different BAQ configurations.

APPENDIX IMPACT OF SAR BACKSCATTER INHOMOGENEITY ON COHERENCE ESTIMATION

Starting from a comment raised by one anonymous reviewer, in this appendix we investigate the influence of SAR image inhomogeneities on the estimate accuracy of the interferometric coherence, as this may impact the coherence degradation shown in Fig. 4 (Section III-B2), and, in turn, the resulting performance-dependent bitrate allocation, according to the approach proposed in this paper. For this purpose, we carried out a set of simulations aimed at assessing the mentioned effects, which are described in the following.

The SAR signal \mathcal{Z} is modeled as complex random process

where real and imaginary part follow a zero-mean Gaussian distribution with variance σ^2

$$\mathcal{Z} = \mathcal{U} + j\mathcal{V}; \quad \mathcal{U} \sim \mathcal{N}(0, \sigma^2), \mathcal{V} \sim \mathcal{N}(0, \sigma^2), \quad (15)$$

being j the imaginary unit. From this, the SAR backscattering coefficient σ^0 is derived as $\sigma^0 = |\mathcal{Z}|^2$.

In this analysis, several one-dimensional SAR backscatter profiles showing a rectangular wave-like texture have been simulated. The texture is characterized by a low power σ^2_{low} and a high power σ^2_{high} level which alternate according to a certain wave frequency f (or period T). The specific values of σ^2_{low} and σ^2_{high} are set depending on the desired degree of heterogeneity in the SAR backscatter σ_{σ^0} , which is expressed as $\sigma_{\sigma^0} = \text{stddev}\{10 \cdot \log_{10}(\sigma^2)\}$ consistently to (12) in Section III-B. On the other hand, different periods T of the rectangular wave have been selected in relation to the window size (or number of looks N_l) used for the coherence estimation. Two exemplary backscatter profiles which have been generated for the present analysis are shown in Fig. 28(a) and Fig. 28(b) for different texture characteristics.

As next step, two interferometric channels \mathcal{M} and \mathcal{S} (master and slave, respectively) with a given correlation (coherence) ρ are simulated assuming

$$\mathcal{S} = \rho \cdot \mathcal{M} + \sqrt{1 - \rho^2} \cdot \mathcal{E}, \quad (16)$$

where \mathcal{M} and \mathcal{E} are modeled as complex i.i.d. zero-mean Gaussian processes $\mathcal{M} \sim \mathcal{N}(0, \sigma^2)$, $\mathcal{E} \sim \mathcal{N}(0, \sigma^2)$, the latter representing the decorrelating signal. For the texture generation, as discussed above the variance of the random process σ^2 can assume the values σ^2_{low} or σ^2_{high} along the simulated SAR backscatter profile, while in case of homogeneous scene a constant σ^2 is assumed. For each samples pair of the simulated profiles \mathcal{M} and \mathcal{S} , the coherence estimate $\hat{\rho}$ is derived considering adjacent

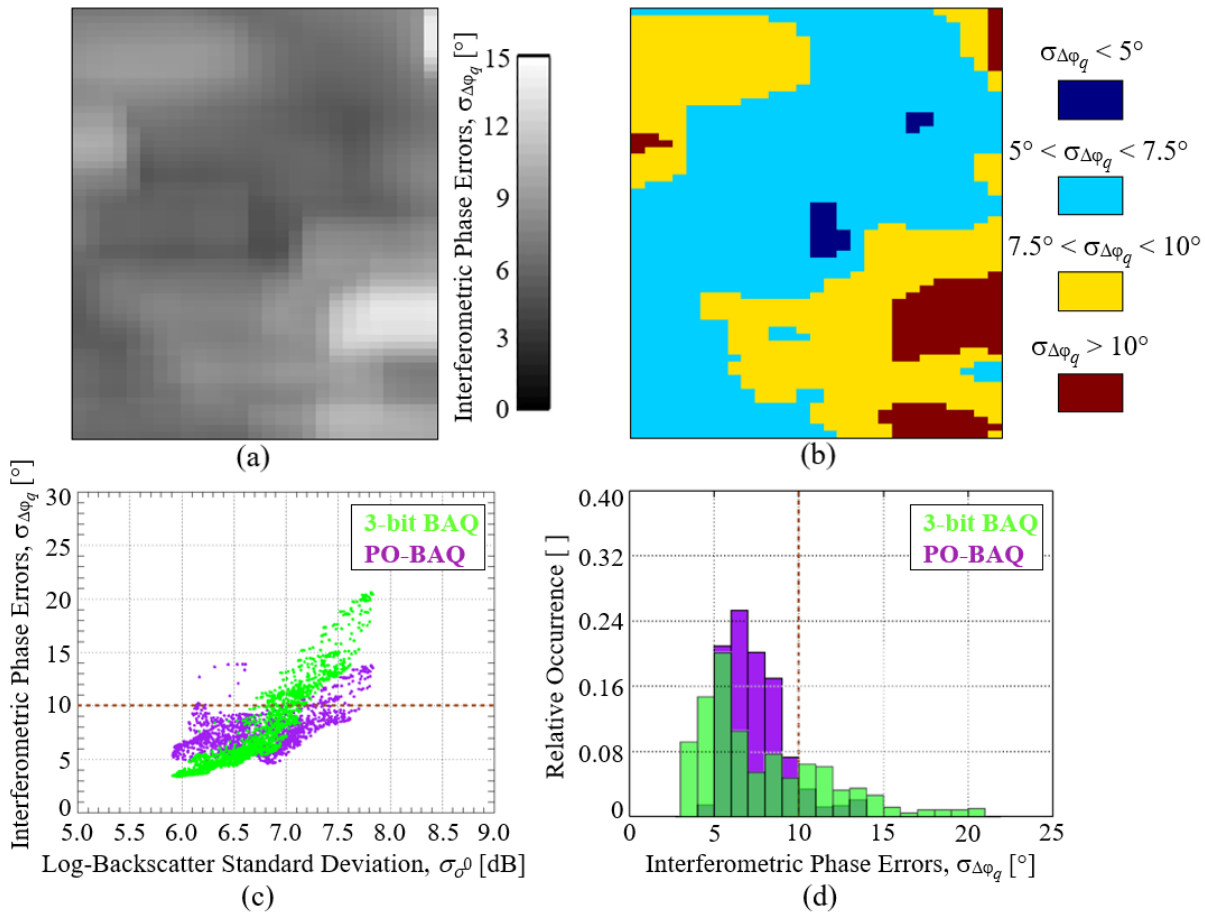


Fig. 25. (a) Phase error map resulting from the bitrate in Fig. 23(b). Each pixel represents the standard deviation of the phase error $\sigma_{\Delta\phi_q}$, calculated in the data block of area A_{SAR} . The pixels which do not fulfill the phase error requirement $\sigma_{\Delta\phi_q, \text{req}} = 10^\circ$ (about 8% of the total) are highlighted in dark red in the mask in (b). (c) Phase error values (taken from the map in (a)) as a function of the standard deviation of backscatter. (d) Corresponding phase error histograms overlaid. The distribution resulting from the 3-bit BAQ (in green) shows a larger dispersion, while the values obtained from the PO-BAQ (in purple) are mostly concentrated between 5° and 10° (depicted in turquoise and yellow in (b)).

samples within a window of size W using the well-known Maximum-Likelihood (ML)-estimator

$$\hat{\rho} = \frac{\sum_{i=1}^W m_i \cdot s_i}{\sqrt{\sum_{i=1}^W |m_i|^2} \sqrt{\sum_{i=1}^W |s_i|^2}}, \quad (17)$$

being m and s the samples of the master \mathcal{M} and slave \mathcal{S} channel, respectively. Fig. 29(a), (c) and (e) show the coherence bias $\beta_\rho = \hat{\rho} - \rho$ as function of the true coherence ρ for different number of looks N_1 and for three different scenarios: homogeneous backscatter (i.e. no texture, constant σ^0 and $\sigma_{\sigma^0} = 1$ dB, Fig. 29(a)), “moderate” texture, modeled with a period of the rectangular wave $T = 5$ times the window estimation size, and $\sigma_{\sigma^0} = 2$ dB (Fig. 29(c)), and “strong” texture, modeled with a period $T = 0.25$ times the window estimation size, and $\sigma_{\sigma^0} = 5$ dB (Fig. 29(e)). A visible increase in the coherence bias for the strong texture case w.r.t. the moderate texture and the homogeneous case can be noticed, especially for low-coherence signals. Indeed, larger texture amplitudes (defined by σ_{σ^0}) in combination with shorter relative texture periods T imply that pixels from

different populations are mixed with each other, ultimately affecting the overall coherence estimation.

Finally, Fig. 29(b), (d) and (f) depict the standard deviation of the coherence estimate for the three considered scenarios (homogeneous, moderate, and strong texture, respectively) and large dispersion are consistently observed for the strong texture case in Fig. 29(f): texture with short wave period w.r.t. coherence estimation window, in combination with large backscatter heterogeneity, causes significant bias/dispersion in the coherence estimate, an aspect which needs to be carefully taken into account for performance prediction and assessment, especially over low-coherence areas and when a limited number of looks $N_1 < 20$ is used for coherence estimation.

REFERENCES

- [1] F. Lee-Lueng and B. Holt, “SEASAT views oceans and sea ice with synthetic aperture radar,” NASA, JPL, Publication 81-120, Feb. 1982.
- [2] D. Massonnet, M. Rossi, C. Carmona, F. Adragna, G. Peltzer, K. Feigl, and T. Rabaute, “The displacement field of the Landers earthquake mapped by radar interferometry,” *Nature*, vol. 364, pp. 138–142, July 1993.

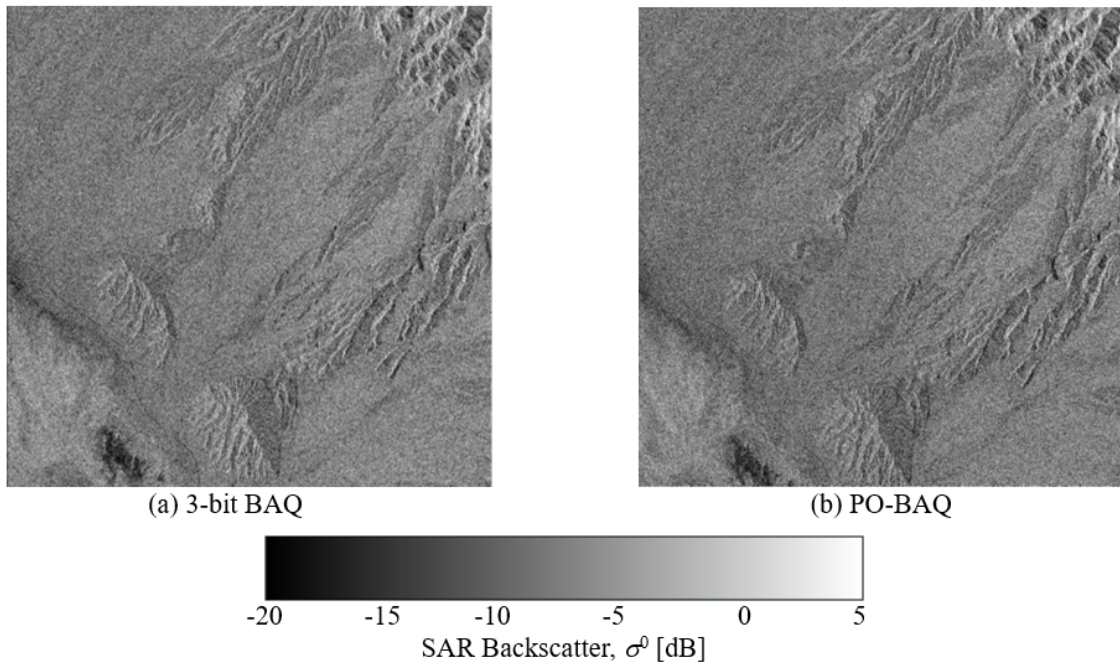


Fig. 26. Radar backscatter σ^0 map of the area delimited in red in Fig. 23(a), obtained by quantizing the raw data with (a) nominal 3-bit BAQ and (b) the considered PO-BAQ with the bitrate map in Fig. 23(b), and no significant difference can be appreciated.

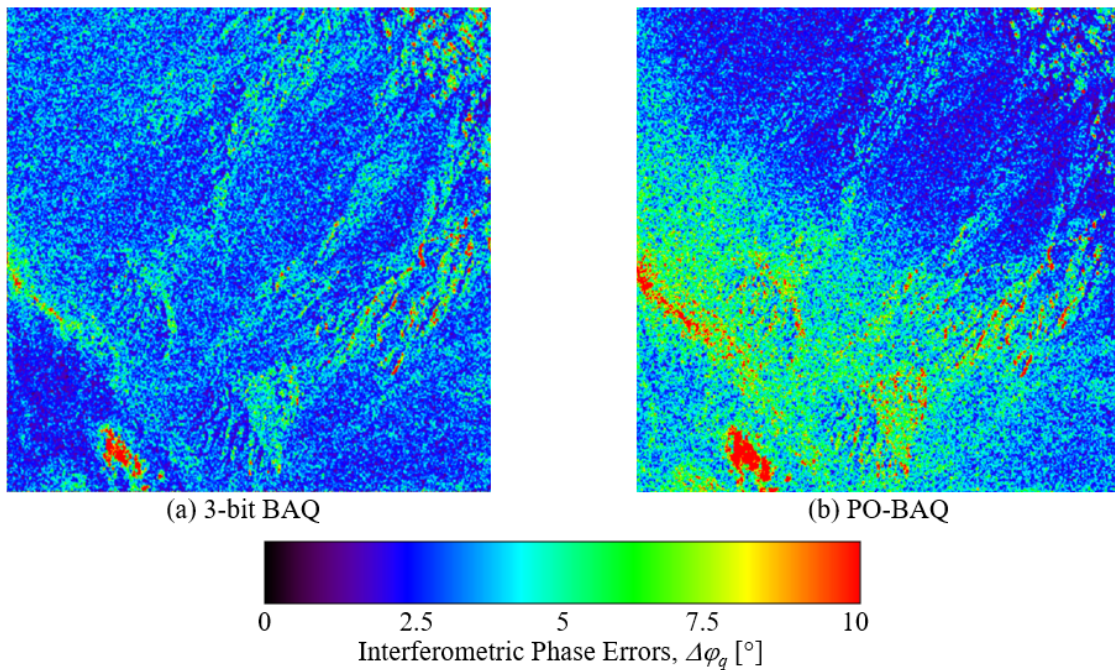


Fig. 27. Map of the interferometric phase errors $\Delta\varphi_q$ of the area delimited in red in Fig. 23(a), obtained by quantizing the raw data with (a) nominal 3-bit BAQ and (b) the considered PO-BAQ with the bitrate map in Fig. 23(b). Visible differences can be noticed as a consequence of using a different bitrate for raw data compression (indeed, for the PO-BAQ case, the bit rate is of between 2 bits/sample and 2.5 bits/sample).

- [3] M. Werner, "Shuttle Radar Topography Mission (SRTM): mission overview," *J. of Telecomm. (Frequenz)*, vol. 55, no. 3, pp. 75–79, March 2001.
- [4] G. Krieger, A. Moreira, H. Fiedler, I. Hajnsek, M. Werner, M. Younis, and M. Zink, "TanDEM-X: A satellite formation for high-resolution SAR interferometry," *IEEE Trans. Geosci. Remote Sens.*, vol. 45, no. 11, pp. 3317–3341, November 2007.
- [5] P. Rizzoli, M. Martone, C. Gonzalez, C. Wecklich, B. Bräutigam, D. Borla Tridon, M. Bachmann, D. Schulze, T. Fritz, M. Huber, B. Wessel, G. Krieger, M. Zink, and A. Moreira, "Generation and performance assessment of the global TanDEM-X digital elevation model," *ISPRS Journal of Photogrammetry and Remote Sensing*, vol. 132, pp. 119–139, Oct. 2017.
- [6] G. Krieger, N. Gebert, M. Younis, and A. Moreira, "Advanced synthetic

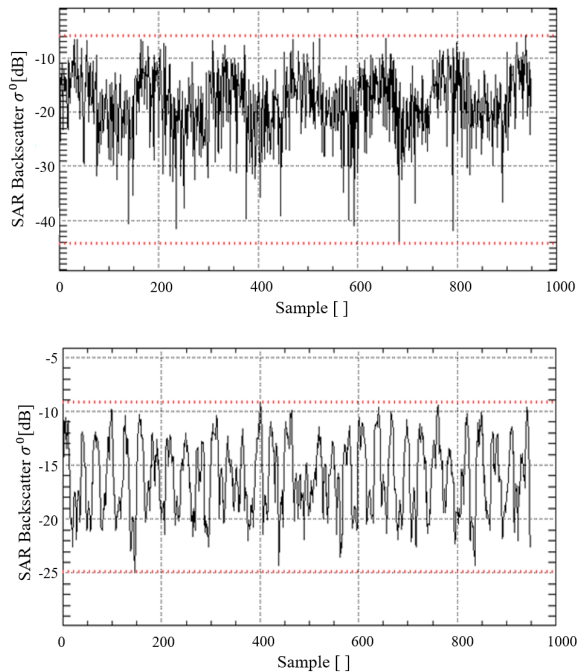


Fig. 28. SAR backscatter profiles used to assess the impact of image inhomogeneities on coherence estimation. (a) σ^0 profile with texture period $T = 5$ times the coherence estimation window (in this case $N_1 = 31$, so the period of the rectangular wave $T \sim 150$ samples) and $\sigma_{\sigma_0} = 5$ dB. (b) σ^0 texture period $T = 1$ coherence estimation window (hence $T \sim 30$ samples) and $\sigma_{\sigma_0} = 3$ dB.

aperture radar based on digital beamforming and waveform diversity,” in *Proc. IEEE Radar Conf.*, Rome, Italy, May 2008, pp. 767–772.

- [7] A. Freeman, G. Krieger, P. Rosen, M. Younis, W. Johnson, S. Huber, R. Jordan, and A. Moreira, “SweepSAR: Beam-forming on receive using a reflector-phased array feed combination for spaceborne SAR,” in *Proc. IEEE Radar Conf.*, Pasadena, CA, USA, May 2009, pp. 1–9.
- [8] A. Currie and M. A. Brown, “Wide-swath SAR,” vol. 139, no. 2, pp. 122–135, 1992.
- [9] G. D. Callaghan and I. D. Longstaff, “Wide swath spaceborne SAR using a quad element array,” vol. 146, no. 3, pp. 159–165, 1999.
- [10] M. Suess, B. Grafmüller, and R. Zahn, “A novel high resolution, wide-swath SAR system,” in *Proc. IGARSS*, Sydney, Australia, July 2001, pp. 1013–1015.
- [11] M. Younis, C. Fischer, and W. Wiesbeck, “Digital beamforming in SAR systems,” *IEEE Trans. on Geosci. and Remote Sens.*, vol. 41, no. 7, pp. 1735–1739, July 2003.
- [12] G. Krieger, N. Gebert, and A. Moreira, “Unambiguous SAR signal reconstruction from non-uniform displaced phase center sampling,” *IEEE Geosci. and Remote Sens. Lett.*, vol. 1, no. 4, pp. 260–264, October 2004.
- [13] N. Gebert, G. Krieger, and A. Moreira, “Digital beamforming on receive: Techniques and optimization strategies for high-resolution wide-swath SAR imaging,” *IEEE Trans. Aerosp. Electron. Syst.*, vol. 45, no. 2, pp. 564–592, April 2009.
- [14] B. Grafmüller and C. Schaefer, “High-resolution synthetic aperture radar device and antenna for one such radar,” US Patent US 8013 778B2, 12 22, 2005.
- [15] G. Krieger, N. Gebert, M. Younis, F. Bordoni, A. Patyuchenko, and A. Moreira, “Advanced concepts for ultra-wide-swath SAR imaging,” in *Proc. EUSAR*, Friedrichshafen, Germany, June 2008, pp. 1–4.
- [16] M. Villano, G. Krieger, and A. Moreira, “Staggered SAR: High-resolution wide-swath imaging by continuous PRI variation,” *IEEE Trans. Geosci. and Remote Sens.*, vol. 52, no. 7, pp. 4462–4479, July 2014.
- [17] M. Villano, G. Krieger, M. Jäger, and A. Moreira, “Staggered SAR: Performance analysis and experiments with real data,” *IEEE Trans. on Geosci. and Remote Sens.*, vol. 55, no. 11, pp. 6617–6638, November 2017.
- [18] F. Queiroz de Almeida, “Multichannel staggered SAR for high-resolution wide-swath imaging,” Ph.D. dissertation, Karlsruhe Institute of Technology, Wessling, Germany, 2017.
- [19] F. Queiroz de Almeida, M. Younis, G. Krieger, and A. Moreira, “Multichannel staggered SAR with reflector antennas: Discussion and proof of concept,” in *International Radar Symposium (IRS)*. IEEE, 2017, pp. 1–10.
- [20] T. Algra, “Data compression for operational SAR missions using entropy-constrained block adaptive quantization,” in *Proc. Int. Geosci. Remote Sens. Symp.*, Toronto, Canada, June 2002, pp. 1135–1138.
- [21] E. Attema, C. Cafforio, M. Gottwald, P. Guccione, A. M. Guarnieri, F. Rocca, and P. Snoeij, “Flexible dynamic block adaptive quantization for Sentinel-1 SAR missions,” *IEEE Geosci. Remote Sens. Lett.*, vol. 7, no. 4, pp. 766–770, October 2010.
- [22] P. Guccione and A. M. Guarnieri, “A space adaptive quantizer for spaceborne SAR,” *IEEE Trans. Geosci. Remote Sens.*, vol. 49, no. 10, pp. 3564–3573, October 2011.
- [23] M. Martone, B. Bräutigam, and G. Krieger, “Azimuth-switched quantization for SAR systems and performance analysis on TanDEM-X data,” *IEEE Geosci. Remote Sens. Lett.*, vol. 11, no. 1, pp. 181–185, January 2014.
- [24] J. Fischer, U. Benz, and A. Moreira, “Efficient SAR raw data compression in frequency domain,” in *IEEE Int. Geosci. Remote Sens. Symp.*, Hamburg, Germany, July 1999, pp. 1034–1037.
- [25] E. Magli and G. Olmo, “Lossy predictive coding of SAR raw data,” *IEEE Trans. Geosci. and Remote Sens.*, vol. 41, no. 5, pp. 977–987, May 2003.
- [26] T. Ikuma, M. Naraghi-Pour, and T. Lewis, “Predictive quantization of range-focused SAR raw data,” *IEEE Trans. Geosci. and Remote Sens.*, vol. 50, no. 4, pp. 1340–1348, April 2012.
- [27] P. Guccione, M. Scagliola, and D. Giudici, “Principal components dynamic block quantization for multichannel SAR,” in *IEEE Int. Geosci. Remote Sens. Symp.*, Beijing, China, July 2016, pp. 2090–2093.
- [28] M. Martone, M. Villano, M. Younis, and G. Krieger, “Efficient onboard quantization for multi-channel SAR systems,” *IEEE Geosci. Remote Sens. Lett.*, vol. 16, no. 12, pp. 1859–1863, 2019.
- [29] M. Villano, G. Krieger, and A. Moreira, “Onboard processing for data volume reduction in high-resolution wide-swath SAR,” *IEEE Geosci. Remote Sens. Lett.*, vol. 13, no. 8, pp. 1173–1177, August 2016.
- [30] M. Martone, N. Gollin, M. Villano, P. Rizzoli, and G. Krieger, “Predictive quantization for data volume reduction in staggered SAR systems,” *IEEE Trans. Geosci. Remote Sens.*, vol. 58, no. 8, pp. 5575–5587, 2020.
- [31] R. Torres, P. Snoeij, D. Geudtner, D. Bibby, M. Davidson, E. Attema, P. Potin, B. Rommen, N. Floury, M. Brown *et al.*, “Gmes sentinel-1 mission,” *Remote Sens. Environ.*, vol. 120, pp. 9–24, 2012.
- [32] V. Syrris, C. Corbane, M. Pesaresi, and P. Soille, “Mosaicking Copernicus Sentinel-1 data at global scale,” *IEEE Trans. on Big Data*, vol. 6, no. 3, pp. 547–557, 2018.
- [33] B. Bauer-Marschallinger, V. Freeman, S. Cao, C. Paulik, S. Schauler, T. Stachl, S. Modanesi, C. Massari, L. Ciabatta, L. Brocca, and W. Wagner, “Toward global soil moisture monitoring with Sentinel-1: harnessing assets and overcoming obstacles,” *IEEE Trans. on Geosci. and Remote Sens.*, vol. 57, no. 1, pp. 520–539, 2018.
- [34] A. Moreira, G. Krieger, M. Younis, I. Hajnsek, K. Papathanassiou, M. Eineder, and F. De Zan, “Tandem-L: A mission proposal for monitoring dynamic earth processes,” in *Proc. Int. Geosci. Remote Sens. Symp.*, Vancouver, Canada, July 2011, pp. 1385–1388.
- [35] A. Moreira, G. Krieger, I. Hajnsek, K. Papathanassiou, M. Younis, P. Lopez-Dekker, S. Huber, M. Villano, M. Pardini, M. Eineder *et al.*, “Tandem-L: A highly innovative bistatic SAR mission for global observation of dynamic processes on the Earth’s surface,” *IEEE Geosci. and Remote Sens. Mag.*, vol. 3, no. 2, pp. 8–23, 2015.
- [36] M. Di Salvo, A. Perrera, M. Degiorgi, A. Ritorto, L. Vinciguerra, F. Temussi, M. Villano, G. Krieger, F. Queiroz de Almeida, J. Reimann, M. Zonno, and M. Younis, “ROSE-L EO system-mission and instrument performance assessment,” in *Proc. ARSI*, 2019.
- [37] M. Davidson, N. Gebert, and L. Giulicchi, “ROSE-L-The L-band SAR Mission for Copernicus,” in *Proc. EUSAR*, 2021, pp. 1–2.
- [38] M. Zonno, J. Matar, F. Q. de Almeida, M. Younis, J. Reimann, M. Rodriguez-Cassola, G. Krieger, A. Perrera, and M. Tossaint, “Sentinel-1 Next Generation: main mission and instrument performance of the Phase 0,” in *Proc. EUSAR*, 2021, pp. 1–5.
- [39] D. Geudtner and M. Tossaint, “Sentinel-1 Next Generation: C-band data continuity and novel capabilities,” in *Proc. EUSAR*, 2021, pp. 1–4.

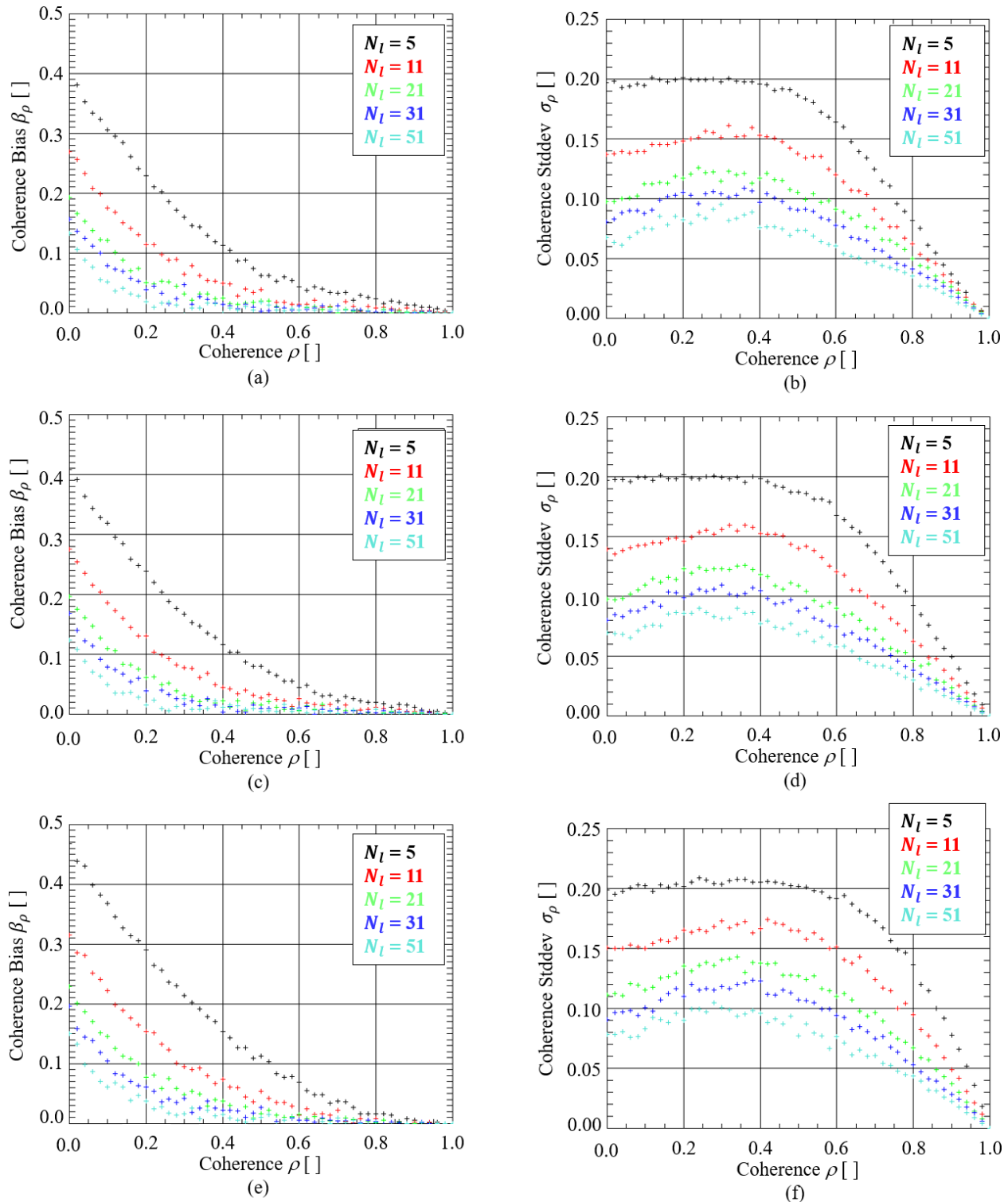


Fig. 29. Coherence bias β_ρ (plots on the left-hand side) and standard deviation σ_ρ (on the right-hand side) as a function of the true coherence calculated for different numbers of looks N_l (depicted in different colors) for: (a)-(b) the homogeneous backscatter scenario ($\sigma_\sigma^0 = 1$ dB); (c)-(d) assuming a rectangular wave with a period $T = 5$ times the window estimation size and $\sigma_\sigma^0 = 2$ dB; (e)-(f) assuming a period $T = 0.25$ times the window estimation size and $\sigma_\sigma^0 = 5$ dB.

[40] N. Jayant and P. Noll, *Digital Coding of Waveforms—Principles and Applications to Speech and Video*. New Jersey: Prentice-Hall, 1984.

[41] D. Lancashire, B. Barnes, and S. Udall, “Block adaptive quantization,” US Patent US 6255987, 07 3, 2001.

- [42] R. Kwok and W. T. K. Johnson, "Block adaptive quantization of Magellan SAR data," *IEEE Trans. on Geosci. and Remote Sens.*, vol. 27, no. 4, pp. 375–383, July 1989.
- [43] S. Huber, M. Younis, and G. Krieger, "The TanDEM-X mission: overview and interferometric performance," *Int. J. Microw. Wireless Technol.*, vol. 2, no. 3–4, pp. 379–389, July 2010.
- [44] M. Martone, B. Bräutigam, and G. Krieger, "Quantization effects in TanDEM-X data," *IEEE Trans. Geosci. and Remote Sens.*, vol. 53, no. 2, pp. 583–597, February 2015.
- [45] J. S. Lee, K. W. Hoppel, S. A. Mango, and A. R. Millerand, "Intensity and phase statistics of multilook polarimetric and interferometric SAR imagery," *IEEE Trans. Geosci. and Remote Sens.*, vol. 32, no. 5, pp. 1017–1028, Sep. 1994.
- [46] M. Zink, G. Krieger, H. Fiedler, I. Hajnsek, and A. Moreira, "The tandem-x mission concept," in *Proc. EUSAR*, Friedrichshafen, Germany, June 2008, pp. 1–4.
- [47] M. Zink, A. Moreira, I. Hajnsek, P. Rizzoli, M. Bachmann, R. Kahle, T. Fritz, M. Huber, G. Krieger, M. Lachaise *et al.*, "TanDEM-X: 10 years of formation flying bistatic SAR interferometry," *IEEE Journal of Selected Topics in Applied Earth Observations and Remote Sensing*, vol. 14, pp. 3546–3565, 2021.
- [48] "The TanDEM-X 90m Digital Elevation Model," <https://geoservice.dlr.de/web/dataguide/tdm90/>, [Online; accessed 04-10-2019].
- [49] J. Mittermayer, M. Younis, R. Metzger, S. Wollstadt, and J. Márquez-Martínez, "TerraSAR-X system performance characterization and verification," *IEEE Trans. Geosci. Remote Sens.*, vol. 48, no. 2, pp. 660–676, February 2010.
- [50] P. Prats-Iraola, M. Rodríguez-Cassola, L. Marotti, M. Nannini, S. Wollstadt, D. Schulze, N. Tous-Ramon, M. Younis, G. Krieger, and A. Reigber, "TAXI: a versatile processing chain for experimental TanDEM-X product evaluation," in *Proc. Int. Geosci. Remote Sens. Symp.*, Honolulu, Hawaii, July 2010, pp. 4059–4062.
- [51] P. Rizzoli, B. Bräutigam, S. Wollstadt, and J. Mittermayer, "Radar backscatter mapping using TerraSAR-X," *IEEE Trans. Geosci. Remote Sens.*, vol. 49, no. 10, pp. 3538–3547, 2011.
- [52] A. Gersho, "Principles of quantization," *IEEE Trans. Circuits Syst.*, vol. 25, no. 7, pp. 427–436, July 1978.
- [53] M. Martone, N. Gollin, P. Rizzoli, and G. Krieger, "Performance-optimized quantization for InSAR applications," in *Proc. EUSAR*, 2021, pp. 1–6.

TABLE IV
ACQUISITION PARAMETERS FOR THE TANDEM-X SCENE OVER DEATH VALLEY (USA) INVESTIGATED IN FIG. 23 TO FIG. 27.

Test Site	Death Valley
Land cover	soil & rock, mountainous
Center coordinates [lat./lon.]	[36.5°N, 116.7°W]
Acquisition date	2012-06-09
Incidence angle, θ_i	40.7°
Backscatter std dev, σ_{σ^0}	3.7 dB
Acquisition mode	Bistatic, stripmap
Polarization channel	HH